This is a preprint, the final version is subject to change, of the American Mineralogist (MSA)
Cite as Authors (Year) Title. American Mineralogist, in press.
(DOI will not work until issue is live.) DOI: http://dx.doi.org/10.2138/am-2016-5728

REVISION 1

Phosphate minerals in the H group of ordinary chondrites, and fluid activity recorded by apatite heterogeneity in the Zag H3-6 regolith breccia

Rhian H. Jones[1,2], Francis M. McCubbin[2,3,4] and Yunbin Guan[5]

[1]School of Earth, Atmospheric and Environmental Sciences, The University of Manchester, M13 9PL, U.K. Rhian.jones-2@manchester.ac.uk

[2]Department of Earth and Planetary Sciences, University of New Mexico, Albuquerque, NM 87131, U.S.A.

[3]Institute of Meteoritics, University of New Mexico, Albuquerque, NM 87131, U.S.A.

[4]NASA Johnson Space Center, Mailcode XI2, 2101 NASA Parkway, Houston, TX 77058, U.S.A. francis.m.mccubbin@nasa.gov

[5]Division of Geological and Planetary Sciences, Caltech, Pasadena, CA 91125, U.S.A. yunbin@gps.caltech.edu

Submitted to American Mineralogist, February 2016: Apatite thematic issue

Revised: June 2016

This is a preprint, the final version is subject to change, of the American Mineralogist (MSA)
Cite as Authors (Year) Title. American Mineralogist, in press.
(DOI will not work until issue is live.) DOI: http://dx.doi.org/10.2138/am-2016-5728

Abstract

Phosphate minerals in ordinary chondrites provide a record of fluids that were present during metamorphic heating of the chondrite parent asteroids. We have carried out a petrographic study of the phosphate minerals, merrillite and apatite, in metamorphosed H group ordinary chondrites of petrologic type 4-6, in order to understand development of phosphate minerals and associated fluid evolution during metamorphism. In unbrecciated chondrites, apatite is Cl-rich and shows textural evolution from fine-grained apatite-merrillite assemblages in type 4 towards larger, uniform grains in type 6. The Cl/F ratio in apatite shows a similar degree of heterogeneity in all petrologic types, and no systematic change in compositions with metamorphic grade, which suggests that compositions in each meteorite are dictated by localized conditions, possibly because of a limited fluid / rock ratio. The development of phosphate minerals in H chondrites is similar to that of L and LL chondrites, despite the fact that feldspar equilibration resulting from albitization is complete in H4 chondrites but not in L4 or LL4 chondrites. This suggests that albitization took place during an earlier period of the metamorphic history than that recorded by preserved apatite compositions, and chemical equilibrium was not achieved throughout the H chondrite parent body or bodies during the late stages of metamorphism. A relict igneous clast in the H5 chondrite, Oro Grande has apatite rims on relict phenocrysts of (possibly) diopside that have equilibrated with the host chondrite. Apatite in the Zag H3-6 regolith breccia records a complex fluid history, which is likely related to the presence of halite in this meteorite. The porous dark H4 matrix of Zag, where halite is observed, has a high apatite / merrillite ratio, and apatite is extremely Cl-rich. One light H6 clast contains similarly Cl-rich apatite. In a second light H6 clast, apatite compositions are very heterogeneous

and more F-rich. Apatites in both H4 matrix and H6 clasts have very low H_2O contents. Heterogeneous apatite compositions in Zag record multiple stages of regolith processing and shock at the surface of the H chondrite parent body, and apatite records either the passage of fluids of variable compositions resulting from different impact-related processes, or the passage of a single fluid whose composition evolved as it interacted with the chondrite regolith. Unraveling the history of apatite can potentially help to interpret the internal structure of chondrite parent bodies, with implications for physical and mechanical properties of chondritic asteroids. The behavior of halogens recorded by apatite is important for understanding the behavior of volatile elements in general: if impact-melt materials close to the surface of a chondritic asteroid are readily degassed, the volatile inventories of terrestrial planets could be considerably more depleted than the CI carbonaceous chondrite abundances that are commonly assumed.

Keywords:

ANALYSIS, CHEMICAL (MINERAL): merrillite, apatite
MAJOR AND MINOR ELEMENTS: merrillite, apatite
METEORITE: ordinary chondrite, H chondrite, Avanhandava, Estacado, Oro Grande, Richardton, Zag
PETROGRAPHY: ordinary chondrite, H chondrite

Introduction

One of the important considerations related to the formation and geological evolution of the terrestrial planets is the initial abundance of volatile species such as water and the halogens: these species can play a major role in determining the geochemical behavior of planetary interiors. Since determinations of bulk compositions of the terrestrial planets are largely based on our understanding of elemental abundances in chondritic meteorites, it is important to understand the behavior of volatile species in these meteorites. For the halogens in particular there are considerable uncertainties and unknowns with respect to their elemental abundances as well as their mineralogical hosts in chondrites (Brearley and Jones 2016). Overall, we have a rather poor understanding of the distribution of the halogens in early solar system materials, and hence in materials that were accreting to form the planets.

The ordinary chondrites (OCs) consist of three groups, H, L and LL, which have all undergone metamorphism on their separate parent bodies (e.g. Huss et al. 2006). The degree of metamorphism is identified by a scheme of petrologic types (Van Schmus and Wood 1967) that range from 3.00 (pristine aggregates of solar nebula materials) to 6 (peak temperatures up to the onset of melting at ~950 °C). Secondary minerals that form during equilibration of OCs include merrillite, apatite, and feldspar (e.g. Brearley and Jones 1998). The phosphate minerals merrillite $[Na_2(Mg,Fe^{2+})_2Ca_{18}(PO_4)_{14}]$ and apatite $[Ca_5(PO_4)_3(X)]$ can provide insights into processes that redistribute halogens in the early solar system, by providing a window into processes that take place on chondritic parent asteroids. Because the X anion site in apatite can host F^-, Cl^-, and OH^-, apatite can provide direct evidence for the presence and relative abundances of volatile species, and hence the nature and role of fluids that existed during the period of metamorphism which

96 took place in the first few million years of solar system history. In a recent study of petrologic
97 type 4-6 LL chondrites, we showed that chlorapatite grains record the presence of
98 metasomatizing fluids throughout the metamorphic history of the LL parent body (Jones et al.
99 2014), and that in at least the late stages of metamorphism, these fluids are dry (water-poor) and
100 halogen-bearing. Metasomatizing fluids are also likely responsible for albitization reactions that
101 produce albitic feldspar in ordinary chondrites (Kovach and Jones 2011; Jones and Brearley
102 2010a,b; Lewis and Jones 2014, 2015, 2016). The three groups of ordinary chondrites all record
103 the effects of similar metamorphic and metasomatic environments. However, there are also
104 significant differences. Feldspar in H4 chondrites is albitic and homogeneous in composition,
105 whereas feldspar in L4 and LL4 chondrites is highly heterogeneous, ranging from almost end-
106 member An to Ab (Kovach and Jones 2011;Lewis and Jones 2016). In L and LL chondrites,
107 equilibration to albitic feldspar is only complete in petrologic type 6. Hence, it appears that
108 complete albitization took place at significantly lower temperatures in the H chondrites (<600 °C
109 for petrologic type 3: Huss et al. 2006) than in the L and LL chondrites, possibly as a result of
110 differences in fluid composition and / or availability. In this study, we examine the occurrence
111 and development of apatite and merrillite in H chondrites, and we address the question of
112 whether phosphate minerals also record differences in the conditions of secondary processing
113 between the parent bodies of H vs. L and LL chondrites.

114 We have also studied the H chondrite regolith breccia fall, Zag. Zag and a similar
115 meteorite, Monahans (1998) (hereafter Monahans) contain indigenous (extraterrestrial) halite
116 (Zolensky et al. 1999; Whitby et al. 2000; Rubin et al. 2002; Bridges et al. 2004). Halite contains
117 low-temperature (<100 °C) aqueous fluid inclusions and is considered to result from evaporation
118 of brines. The source of water has variously been proposed to be exogenous water delivered to

the parent body by cometary or asteroidal ice fragments (Zolensky et al. 1999; Bridges et al. 2004), dehydration of the asteroid interior (Whitby et al. 2000), or impact heating of phyllosilicates (Rubin et al. 2002). Alternatively, halite may be exogenous, derived from either a carbonaceous asteroid such as Ceres (Fries et al. 2014; Yurimoto et al. 2014) or via cryovolcanism on a body such as the Saturnian satellite Enceladus (Zolensky et al. 2013). We have studied the phosphate mineralogy of Zag, in order to examine whether apatite can help shed light on the conditions that led to halite formation and halogen redistribution in the regolith of the H chondrite asteroid.

Samples and Methods

We studied phosphate minerals in Avanhandava (H4), Richardton (H5), Oro Grande (H5) Estacado (H6), and Zag (H3-6) (Table 1). Phosphate minerals were identified and analyzed in the following thin sections: Avanhandava, UNM 88; Richardton, UNM 384; Oro Grande, UNM 55; Estacado, UNM 609; and Zag, UNM 1136. Oro Grande is a find and is moderately weathered; the others are falls. All the samples have nominally low shock levels, between S1 and S3 (Stöffler et al. 1991; Rubin 1994, 2002, 2004; Folco et al. 1996; Grossman 1999). The Zag thin section we studied contains both dark matrix and light clast lithologies.

We used WDS/EDS X-ray mapping to locate phosphate mineral grains, using the JEOL 8200 electron microprobe at the University of New Mexico (UNM). For mapping, we typically used a defocused electron beam, 10 μm in diameter, and a counting time of 20 milliseconds per pixel, in order to minimize volatile loss from susceptible phases. Back-scattered electron (BSE) images were obtained using the electron microprobe and the JEOL 5800LV SEM at UNM, as

well as an FEI XL30 ESEM-FEG at the University of Manchester. We determined modal abundances of phosphate minerals from X-ray maps using the ImageJ image analysis program (Schneider et al. 2012). Modal abundances of total phosphates were determined from P X-ray maps, modal abundances of Cl-apatite were determined from Cl X-ray maps, and modal abundances of merrillite were calculated by subtracting the abundance of Cl-apatite from total phosphates. Estimated errors for modal abundances determined with this method are less than 10% relative.

Electron microprobe analyses of merrillite and chlorapatite were obtained using the JEOL 8200 electron microprobe. We used conditions that were designed to minimize volatilization of halogens (F and Cl) in chlorapatite: operating conditions were 15kV and a 20nA beam current, and we used a defocused (usually 5 μm) electron beam to analyze both standards and unknowns. The problem of fluorine migration in apatite under the electron beam has been recognized in previous studies (Stormer et al. 1993; McCubbin et al. 2010a, 2011). We monitored the F and Cl count rates during analyses using the live chart recorder on the electron microprobe and discarded analyses in which we observed significant changes in F and/or Cl counts during peak counting times. The following standards were used for calibration: Taylor apatite and Apatite 020 (see below) for Ca, P, and F (McCubbin et al. 2012); sodalite for Na and Cl, Taylor olivine for Mg and Fe, and Y and Ce end-member phosphates for Y and Ce. Detection limits for F and Cl were 0.04 and 0.01 wt% respectively, and detection limits for Y_2O_3 and Ce_2O_3 were 0.05 wt%. Detection limits for all other elemental oxides were 0.01 or 0.02 wt%. For apatite analyses, we defined criteria for an acceptable analysis where each cation site is populated by ±2% of values in the ideal structural formula. Thus an acceptable analysis was defined as follows: Total oxide wt% between 97 and 102; Sum of tetrahedral site cations

(ΣTetrahedral) between 2.94 and 3.06; Sum of octahedral site cations (ΣOctahedral) between 4.9 and 5.1. For Oro Grande only, most analyses fitted all criteria except for (ΣTetrahedral) which was relaxed to values lying between 4.9 and 5.15. For several analyses in Richardton, the total structural formulae values for F+Cl were slightly >1: for these analyses only, Cl was calculated as Cl = 1-F (c.f. McCubbin et al. 2013).

Secondary ion mass spectrometry (SIMS) analyses of volatile anion elements (H, F, and S) were obtained using the Cameca IMS 7f-GEO ion microprobe at Caltech. Samples were measured with a ~20 μm Cs^+ primary beam of +10 keV and ~3.5nA, rastering over an area of 10x10 μm. Negative secondary ions ($^{12}C^-$, $^{16}O^1H^-$, $^{18}O^-$, $^{19}F^-$, $^{31}P^-$, $^{32}S^-$, and $^{35}Cl^-$) of -10 keV were collected from the center 10 μm at a mass resolving power of ~4500. Sample charging was compensated with an electron gun at -10 keV. Secondary ion images of $^{12}C^-$, $^{16}O^1H^-$, and $^{19}F^-$ were examined before each sample measurement to avoid cracks and contamination. A calibration curve for OH was determined from five terrestrial apatite standards that had H_2O contents varying from 300 to 5500 ppm (McCubbin et al. 2010b, 2012; Jones et al. 2014). A calibration curve for S, based on the five apatite standards, was determined by Jones et al. (2014). SIMS analyses of F in this study show an excellent correlation with electron microprobe and bulk analyses of F abundances, measured in terrestrial standards and apatite grains in LL chondrites (Jones et al. 2014).

Results

Non-brecciated H chondrites

Abundances and distributions of phosphate minerals. Distributions and sizes of phosphate grains in Avanhandava, Oro Grande, Richardton and Estacado are illustrated in the P and Cl X-ray maps shown in Fig. EA1. Abundances of phosphate mineral grains in each chondrite, determined using ImageJ software, are summarized in Table 1. The total abundance of phosphate minerals (apatite + merrillite) is similar in all four chondrites, 0.4-0.5 vol%, but the apatite / merrillite ratio is highly variable, ranging from 0.4 to 1.5. Both minerals are distributed evenly throughout the thin sections studied, although there is some heterogeneity on a scale of millimeters that could account for the observed differences in apatite / merrillite ratios. A large inclusion in Oro Grande that contains apatite is described in more detail below.

Textures of phosphate minerals in Avanhandava, Richardton and Estacado. Figures 1, 2 and 3 illustrate textures of phosphate minerals in the H4-5-6 petrologic sequence represented by Avanhandava, Richardton and Estacado respectively. In all cases, both apatite and merrillite occur as irregularly shaped grains up to 200 μm in length. In Avanhandava (H4), both apatite and merrillite are commonly fragmented into small angular pieces (Fig. 1a). The two minerals can be associated (Fig. 1a), and both are commonly associated with metal / sulfide grains (Fig. 1a-c). Grains of merrillite up to 200 μm in length also occur along and close to the perimeter of relict chondrules (Fig. 1c,d). In Richardton (H5), large apatite grains up to 200 μm in length often contain a small inclusion of merrillite (Fig. 2a,b). Similar to Avanhandava, both apatite and merrillite are commonly associated with metal / sulfide grains (Fig. 2a-d). Apatite grains occur in intergrowths with olivine, in which case they contain rounded olivine inclusions and show a curved interface, concave to the apatite (Fig. 2a,c). Several grains of both apatite and merrillite are connected to vein-like networks of similar material (Fig. 2a,c). In Estacado (H6), apatite and merrillite grains are more angular than those in Richardton, and do not contain many inclusions

of olivine or any merrillite inclusions (Fig. 3). Associations between both phosphate minerals and metal / sulfide grains are common, but many grains of both minerals occur independently of metal in the plane of the thin section. Phosphate minerals occur in the vicinity of chromite-plagioclase assemblages: in the example in Fig. 3d, a merrillite grain is located at the periphery of a chromite-plagioclase assemblage in association with metal / sulfide.

Oro Grande host and igneous inclusion. In the Oro Grande H5 chondrite host, both apatite and merrillite occur as grains up to 200 μm in length, many of which are associated with metal / sulfide grains (Fig. 4). Apatite and merrillite are closely associated (Fig. 4c), and in some grains appear to show a reaction relationship (Fig. 4a,d). Also, some apatite grains contain what appear to be pores (Fig. 4d). Both minerals are present along and close to the boundary of a large (5 mm) inclusion within the H chondrite host (Fig. 4c,d). This inclusion has previously been described as an igneous inclusion that has equilibrated with the host chondrite (Fodor et al. 1972; Jones 2007). The inclusion is dominated by a fine-grained mixture of barred olivine and plagioclase, with olivine bar widths <10 μm (Fig. 4c,d; 5a,b). Throughout the inclusion there are also numerous objects (~50 vol%) that appear to be pseudomorphs of euhedral phenocrysts, 100 to 500 μm in length, which have complex internal textures. Some pseudomorphic regions are dominated by diopside, with minor low-Ca pyroxene and plagioclase, and rims of plagioclase. Apatite occurs as ~20 μm wide rims on these features, between the core region and plagioclase. Other euhedral pseudomorphic regions consist of fine-grained intergrowths of low-Ca pyroxene, diopside, olivine, plagioclase, pigeonite and minor chromite. These regions have thin rims of diopside, overgrown with plagioclase. Throughout the inclusion, iron metal and troilite are minor phases, and chromite is present as ubiquitous but finely dispersed sub-micrometer crystals. Compositions of all phases are essentially identical to those in the host chondrite, and are typical

of equilibrated H chondrites, with average compositions as follows: olivine, Fa_{18}; low-Ca pyroxene, $En_{82}Fs_{17}Wo_1$; diopside, $En_{48}Fs_6Wo_{46}$; feldspar, $An_{12}Ab_{82}Or_6$ (Jones 2007).

Phosphate mineral compositions. Merrillite compositions are close to the ideal formula, $Na_2(Mg,Fe^{2+})_2Ca_{18}(PO_4)_{14}$, in all the H chondrites studied (Table 2: individual analyses are given in Table EA1). Apatite compositions, $Ca_5(PO_4)_3(X)$, have variable Cl/F ratios and each of the chondrites has a distinct average Cl/F ratio: 9.1, 19.5, 6.2 and 14.4 wt% ratio, or 4.9, 10.2, 3.3 and 7.7 atomic ratio, in Avanhandava, Richardton, Oro Grande (host) and Estacado, respectively (Table 3: individual analyses are given in Table EA2). We also define a value of Cl# = Cl/(Cl+F) (atomic), which has a value of 0.83, 0.91, 0.77, 0.89 for these four chondrites, respectively. Figure 6a shows anion site occupancy for all apatite analyses in these four non-brecciated H chondrites. Apatite analyses contain up to 0.15 atoms per formula unit (apfu) "other" than halogens: we have shown that for LL chondrites, this component is not OH^- (Jones et al. 2014), so we label it as "other" rather than the conventional OH^- in this diagram (see also the discussion of the Zag data below). For each chondrite, there is considerable variability in apatite compositions around the chondrite mean, for example Cl# values in Richardton vary in the range 0.85 to 0.97. Apatite compositions in the Oro Grande igneous inclusion are very similar to compositions in the H5 host (Table 3, Table EA2). For all apatite analyses, Y_2O_3 and Ce_2O_3 contents are close to or below detection limits. These elements are not included in Table 3, but are given in Table EA2.

The Zag H3-6 regolith breccia

Petrography. Zag is a regolith breccia that contains mainly light-colored metamorphic clasts, and some dark clasts, set within a dark clastic matrix (e.g. Rubin et al. 2002). The thin

section of Zag we studied (UNM 1136) includes both dark and light material (Fig. 7a). The dark matrix includes clearly defined chondrules and unequilibrated low-Ca pyroxene, and although it is possibly clastic, with some regions showing a higher degree of recrystallization to petrologic type 5, we describe it here as H4 matrix. There are two light regions (clasts) within the thin section, both of petrologic type H6, in which chondrules are poorly defined: H6-1 is a large area, approximately half of the total area, and H6-2 is a smaller area on the left hand side of Fig. 7a. Fig. 7b shows the boundary between dark matrix and H6-2 material: H6-2 contains very few fine-grained metal / sulfide particles compared with the H4 matrix. Figures 7c-f show X-ray maps for an area that consists of approximately equal areas of matrix and H6-1 material. The Fe map does not distinguish the two areas clearly, but the S map shows fine-grained sulfides disseminated throughout the matrix, and larger sulfide grains in H6-1. The finely disseminated sulfides are likely responsible for darkening in the matrix. Rubin et al. (2002) observed extensive silicate darkening within this material, in the form of veinlets of troilite and curvilinear trails of troilite blebs cutting through olivine and pyroxene grains, but in our thin section such linear features are not abundant and fine-grained sulfides more typically occur at silicate grain boundaries (Fig. 8).

The distribution of phosphate minerals is very different in the H4 and H6-1 regions: this is illustrated in the P and Cl X-ray maps of Fig. 7e,f and summarized in Table 1. In the H4 matrix, the abundance of both phosphate minerals is low compared with other H chondrites (total of 0.28 vol%), and apatite is much more abundant than merrillite (apatite / merrillite ratio of 4.6). In contrast, in H6-1, the abundance of both phosphates is much higher (total of 0.64 vol%), and merrillite is much more abundant than apatite (apatite / merrillite ratio of 0.16). Also, merrillite

grains are much larger in H6-1 compared with H4 matrix: many grains are >100 μm across and the largest grains are ~250 μm across in H6-1.

Textures of apatite and merrillite grains in the H4 matrix are illustrated in Fig. 8. Abundant apatite grains, up to about 100 μm across, are mostly irregular in shape. Most apatite grains are not associated with metal. One of the apatite grains in Fig. 8c has a vein-like protuberance into surrounding material. Merrillite occurs as small, mostly <20 μm, rounded or subhedral grains throughout the H4 lithology (Fig. 8b,c), and can be associated with metal (Fig. 8a).

In the H6-1 region, both merrillite and apatite grains are very irregular in shape (Fig. 9). Large merrillite grains >100 μm across are common (Fig. 9a,b), and some show faint features that appear to be multiple parallel sets of striations that could be crystallographically controlled (Fig. 9b). Apatite can occur as independent grains (Fig. 9c), but can also occur intergrown with merrillite (Fig. 9d). Two occurrences of apatite-merrillite-chromite assemblages were observed: in the one illustrated in Fig. 9e, apatite encloses an olivine core and the assemblage is adjacent to an Fe,Ni metal grain.

The H6-2 light clast differs significantly from H6-1. Abundant large apatite grains, typically 100 μm (Fig. 7b) but one over 400 μm across (Fig. 9f), are distributed throughout the H6-2 region. The large apatite grain in Fig. 9f encloses a region of merrillite close to the centre.

In a few areas within both H4 matrix and H6-1, merrillite and sometimes apatite grains are observed along linear features (Fig. 10). These features could either be the result of fluid flow along fractures, or possibly impact melt veins, as discussed below. In the example in Fig. 10a, merrillite is distributed throughout a sinuous feature that has a high concentration of plagioclase, and which contains a chromite-plagioclase assemblage surrounded by merrillite

(Fig. 10b). The merrillite grain in the top left of Fig. 1b shows evidence of flow around the chromite-plagioclase assemblage. We also observed other textures where phosphate minerals in H6-1 appear to have undergone melting in association with plagioclase. The large apatite grain in Fig. 10c shows evidence for incipient melting where it is in contact with plagioclase. The equigranular assemblage shown in Fig. 10d consists of low-Ca pyroxene, Ca-rich pyroxene and plagioclase, with fine-grained (<5 μm) merrillite distributed along grain boundaries. We interpret this texture as a region that has undergone melting and recrystallization, possibly while entrained in an impact-generated melt.

Mineral compositions. Merrillite compositions in Zag are close to the ideal formula, $Na_2(Mg,Fe^{2+})_2Ca_{18}(PO_4)_{14}$, and there are no significant differences between compositions in the two H6 clasts (Table 2). We did not obtain any merrillite analyses in the H4 lithology. In contrast, the different lithologies have distinct apatite compositions (Table 3, Fig. 6b). Apatite in H4 and H6-2 is very chlorine-rich; the most Cl-rich grains, in H4 matrix, contain 6.2 wt% Cl and only 0.03 wt% F, with Cl# = 0.99. Two analyses in the H6-2 clast have lower Cl/F ratios (Fig. 6b): this appears to reflect compositional heterogeneity within individual apatite grains. In the H6-1 clast, apatite is considerably more F-rich and shows a wide range of Cl/F ratios. The most F-rich grain contains 2.9 wt% Cl and 1.9 wt% F, Cl# = 0.45, and the most Cl-rich grain contains 4.7 wt% Cl and 0.8 wt% F, Cl# = 0.76. There are no apparent differences in texture that distinguish high-F apatite grains. Apatite in the mixed apatite / merrillite grain shown in Fig. 9d is F-rich, with F = 1.6 to 1.9 wt%, Cl# = 0.46 to 0.54. Electron microprobe analyses of apatite indicate a significant component of "other" anions, up to 0.13 apfu, in addition to the halogens F and Cl (Fig. 6). In general, compositions with high F contents have higher (F+Cl) anion totals and a lower "other" component.

SIMS analyses of apatite in Zag show very low H_2O abundances, in the range 350-600 ppm, irrespective of the lithology (Table 4). These are maximum values, because many apatite grains in Zag have fine fractures (Fig. 8, 9) that likely contain C and OH contaminants. Also, we measured the background abundance on a merrillite grain in the same session, and obtained a value of 744 ppm. The high background resulted from strong outgassing of the thin section, and short residence time in the vacuum. As a result, the H_2O abundances we obtained for apatite should be considered to be below the detection limit. Although our measurements cannot be considered quantitative, we can confidently state that H_2O abundances are low, and significantly lower than 1000 ppm. This H_2O abundance clearly does not entirely account for the amount of the "other" anion determined from our EPMA analyses: for OH^-, 0.1 apfu would correspond to 1800 ppm H_2O.

Sulfur abundances determined by SIMS are also low, <200 ppm (Table 4). The background S content measured on merrillite is <30 ppm. Neither OH nor S abundances correlate with F content. F contents measured by SIMS are consistent with EPMA analyses on the same grains.

Discussion

Non-brecciated H chondrites

Origin of phosphate minerals: Metamorphism and metasomatism. Phosphate minerals show textural differences in different chondrites, which can be interpreted as progressive textural equilibration with increasing petrologic type. In the H4 chondrite, Avanhandava, apatite occurs in fine-grained assemblages, commonly in association with merrillite (Figs. 1a,b). By petrologic type 5 (Richardton, Oro Grande), apatite grains are larger

and more uniform in appearance, but retain islands of merrillite (Figs. 2, 4), and in petrologic type 6 (Estacado), apatite grains are smooth and uniform in appearance with little evidence of association with merrillite. Merrillite shows less textural evolution, although merrillite regions are more fractured and fine-grained in H4 (Fig. 1) than in H5 and H6 (Figs. 2 and 3). In all the H chondrites, there is a notable association of phosphate minerals with metal grains, consistent with derivation of P from its initial source dissolved in metal (Rubin and Grossman, 1985; Zanda et al. 1994; Jones et al. 2014; McCubbin and Jones 2015). Possible sources of halogens could include chondrule mesostasis glass or chondrite matrix (Jones et al. 2014).

Textural changes through the sequence of petrologic types could be interpreted as occurring in the solid state as a result of diffusive equilibration of the host chondrite assemblage, and are most likely at least partly attributable to this process. However, there is evidence for fluid-derived growth in the form of vein-filling phosphate minerals such as those illustrated in Figs. 1a,b, 2a,c, and 4d, as well as porosity in a limited number of grains (e.g. Fig. 4d). Also, compositional heterogeneity of apatite within each H chondrite (Fig. 6a) suggests that compositions are dictated by localized conditions, possibly because of a limited fluid / rock ratio, which argues against diffusive equilibration over a scale of centimeters. Differences in apatite compositions among individual H chondrites (Fig. 6a), and the lack of a systematic trend in Cl/F ratio with petrologic type, argue that chemical communication was limited within the H chondrite parent body, and that chemical equilibrium was not achieved throughout the body. This observation contrasts with essentially complete equilibration of feldspar throughout petrologic types 4, 5, and 6 (Kovach and Jones 2011) and suggests that apatite compositions record a later stage of the metamorphic history than albitization reactions which appear to have been completed before type 4 conditions were reached. In terms of late-stage fluids recorded in

apatite, we infer that the H chondrite parent body was heterogeneous, which could be the result of limited availability of fluid, or differences in the mechanism for generation of fluid. Alternatively, there could have been multiple H chondrite parent bodies that evolved in a similar manner but with different compositions of late-stage fluids, specifically with different Cl/F ratios. However, the entire range of Cl/F ratios observed for H chondrites is encompassed within a single regolith breccia, Zag, which almost certainly represents a sample from a single parent body. The ordinary chondrite parent bodies also show heterogeneity in oxidation state on a kilometer scale and oxygen isotope compositions on a 100-km scale (Rubin et al. 2008).

Comparison of H chondrites with L and LL chondrites. A comparison of the distribution and occurrence in phosphate minerals among the different OC groups allows us to consider differences in the metasomatic / metamorphic environment on the three parent bodies. Abundances of phosphate minerals in petrologic type 4-6 chondrites of the three OC groups are very similar, mostly totaling between 0.4 – 0.5 vol.% (Table 1; Jones et al. 2014; Lewis and Jones 2016). In all three groups, total phosphate abundance is low in type 4 compared with types 5 and 6. However, the ratio of apatite / merrillite varies widely and shows no systematic relationship with either petrologic type or OC group: values for this ratio that we have observed range from 0.4-1.5 in H chondrites (Table 1), 0.25 – 1.0 in L chondrites (Lewis and Jones 2016) and 0.1 to 0.5 in LL chondrites (Jones et al. 2014). The wide range in apatite / merrillite ratios most likely results from the heterogeneity in distribution of apatite on the scale of a thin section.

Textural equilibration of both apatite and merrillite through the petrologic sequence of H chondrites, described above, is also generally observed in LL chondrites (Jones et al. 2014; McCubbin and Jones 2015). and L chondrites (Lewis and Jones 2016).Also, in all three OC groups, phosphate minerals occur in association with chromite-plagioclase assemblages (Fig. 3d;

393 Jones et al. 2014; Lewis and Jones 2016). These assemblages are considered to be a shock
394 feature (Rubin 2003): if they represent low degrees of partial melting of the host chondrite, it is
395 likely that phosphate minerals would dissolve in the melt and re-precipitate as the melt pocket
396 cools (Jones et al. 2014). Phosphate minerals in association with chromite-plagioclase
397 assemblages do not appear to have notably different compositions to grains that are located
398 elsewhere in the chondrite, which suggests that either melting and crystallization resulted in the
399 same compositions, or that any compositional differences resulting from formation in a small
400 impact melt pocket have been overprinted by later metamorphic or/and metasomatic processes.
401 Overall, phosphate minerals do not appear to record a significant difference in the
402 metamorphic environment between the H vs. L and LL groups, unlike feldspar, and the
403 phosphate minerals in petrologic type 4-6 H chondrites shed little light on different conditions
404 that might have prevailed on the H vs. the L and LL parent bodies. Apatite in H chondrites tends
405 to be more Cl-rich than apatite in L and LL chondrites (Fig. 6a; Jones et al. 2014; Lewis and
406 Jones 2016). However, there is considerable overlap between H and L apatite compositions in
407 the anion ternary diagram (Lewis and Jones 2016), and given the heterogeneity both within each
408 OC group and among groups, the difference is not resolvable. Relationships between the
409 different OC groups are therefore complicated. Our interpretation is that there is decoupling of
410 the period during which extensive albitization took place from the period recorded by preserved
411 apatite compositions, which is likely to be the case if apatite compositions are determined at a
412 late stage of the metamorphic history of the different parent bodies, possibly during cooling.
413 **Igneous inclusion in Oro Grande.** Igneous or lithic inclusions have been described in
414 numerous ordinary chondrites (Hutchison et al. 1988; Bridges and Hutchison 1997; Ruzicka et
415 al. 1998, 2000, 2012). These are igneous-textured inclusions, large relative to chondrules, which

416 often have low abundances of metal and sulfides. There are several different proposed origins for
417 the melts, including shock, vapor condensation, and melts derived from differentiated
418 planetesimals (e.g. see Ruzicka et al. 2012). Igneous inclusions in the L6 chondrite Barwell have
419 I-Xe ages 4565-4566 Ma, suggesting they formed on a parent body that differentiated prior to
420 formation of chondrites (Hutchison 1988; Gilmour et al. 2000; Crowther et al. 2014). The
421 inclusion in Oro Grande is broadly similar to several previously described inclusions, for
422 example Fodor and Keil (1976) described an inclusion with olivine phenocrysts and an
423 interstitial spinifex texture in the Eva H5 chondrite, and Ruzicka et al. (2012) described an
424 inclusion with a porphyritic texture in Buzzard Coulee (H4). Fodor et al. (1972) interpreted the
425 Oro Grande inclusion as an impact melt formed from the silicate portion of equilibrated H5
426 material. However, X-ray mapping (Fig. 5) highlights features that resemble textures seen in
427 terrestrial porphyritic volcanic rocks: we suggest that the fine-grained pseudomorphic features
428 represent aggregates of euhedral phenocrysts that have undergone decompositional breakdown
429 reactions, possibly as a result of shock (Jones 2007). The original porphyritic igneous rock could
430 have contained olivine and / or pyroxene phenocrysts, possibly diopside and pigeonite, which
431 broke down into multi-phase assemblages. Also as a result of the shock, an olivine / plagioclase
432 impact melt was generated, which was injected among the phenocryst clusters and quenched into
433 a barred olivine texture. Chemical equilibration of the inclusion with the Oro Grande host
434 chondrite indicates that formation of the original porphyritic rock, as well as the proposed impact
435 event, and incorporation into the H chondrite host, must have occurred prior to H chondrite
436 parent body metamorphism.

437 The origin of the chlorapatite grains that surround pseudomorphs dominated by diopside
438 is not clear. Possibly, Ca for the chlorapatite originated in diopside, which could have reacted

439 with a P- and Cl-bearing melt or fluid during the impact event that melted the inclusion. Since
440 formation of the inclusion has been overprinted by metamorphic equilibration with the host H5
441 chondrite, it is difficult to speculate further.
442
443 **The Zag H3-6 regolith breccia**
444 **Phosphate minerals: Comparison with unbrecciated H chondrites.** In Zag, the
445 distribution and grain sizes of phosphate minerals differs significantly between the type 4 matrix
446 and type 6 clast lithologies (Fig. 7). We can compare the phosphate occurrences in the different
447 Zag lithologies with non-brecciated chondrites of comparable petrologic type.
448 For the H4 matrix lithology of Zag, both merrillite and apatite consist predominantly of
449 individual grains, and apatite grains tend to be larger (several tens μm) than merrillite grains
450 (typically <20 μm) as well as significantly more abundant (apatite / merrillite ratio of 4.6) (Figs.
451 7,8). This distribution is markedly different from Avanhandava (H4), in which the apatite /
452 merrillite ratio is 0.7 (Table 1), apatite consists of fine-grained aggregates that are commonly
453 associated with merrillite, and merrillite occurs as large grains up to 200 μm (Fig. 1). The apatite
454 / merrillite ratio in Zag H4 matrix material is the highest of all we have measured in our studies
455 of type 4-6 ordinary chondrites: all apatite / merrillite ratios are <1 in LL and L chondrites
456 studied by Jones et al. (2014) and Lewis and Jones (2016). We attribute the high apatite /
457 merrillite ratio to the fact that the H4 material in Zag is a regolith component that has seen a
458 more complex history than a typical petrologic type 4 H chondrite. Apatite compositions in the
459 H4 lithology are mostly very Cl-rich (Fig. 6b), with higher Cl/F ratios than Avanhandava (H4),
460 up to compositions containing almost no F. Although apatite in the H chondrites in general are

quite Cl-rich (Fig. 6a), these Zag compositions are the most Cl-rich of all the OCs we have studied.

We examined two clasts with type 6 lithology, H6-1 and H6-2. In both, merrillite is much more abundant than apatite (apatite / merrillite ratio of 0.16 in H6-1), and grains of both apatite and merrillite are large, up to 200 μm (Fig. 9). Also, intergrowths of apatite and merrillite are observed (Fig. 9d,f). Occurrences of both minerals are similar to those observed in Estacado (H6: Fig. 3), although intergrowths are more similar to Richardton (H5: Fig. 2). The abundance of merrillite and the apatite / merrillite ratio differ from the non-brecciated H chondrites, but since these values have a wide range (0.4-1.5: Table 1), it is not meaningful to attach much significance to these differences. Despite comparable petrographic observations, apatite compositions in the two H6 clasts differ significantly. In the H6-2 clast, apatite compositions are Cl-rich and comparable to the H4 matrix lithology (Fig. 6b). In contrast, in the H6-1 material, apatite compositions are highly heterogeneous, much more F-rich, and compositions extend to lower Cl/F (atomic) ratios of around 1.

The overall picture of apatite in Zag is complex. The H4 and H6-2 clasts have apatite compositions that are close to normal for H chondrites, but the high apatite/merrillite ratio in H4 is unusual. In H6-1, apatite petrography can be considered to be normal, but compositions are heterogeneous and F-rich. Interpreting the evolution of this regolith breccia requires an understanding of these observations, as well as an understanding of the relationship between apatite and halite: since halite is also a halogen-bearing mineral, it is important to question whether the two minerals have a common source.

Relationship between apatite and halite. Halite in Zag, as well as in the related H5 chondrite, Monahans, is demonstrably pre-terrestrial (Zolensky et al. 1999; Whitby et al. 2000; Rubin et al. 2002; Bridges et al. 2004). Previous studies have shown that halite occurs predominantly within the dark matrix of these two chondrites, as grains a few hundred microns across (Zolensky et al. 1999; Whitby et al. 2000; Rubin et al. 2002; Bridges et al. 2004). Halite in both Zag and Monahans contains low-temperature (<100 °C) aqueous fluid inclusions, and is considered to result from evaporation of brines (Zolensky et al. 1999; Whitby et al. 2000; Rubin et al. 2002). In Monahans, halite also contains inclusions of sylvite (KCl) (Zolensky et al. 1999). Halides in both Zag and Monahans have been dated by K-Ar, Rb-Sr and I-Xe methods (Zolensky et al. 1999; Bogard et al. 2001; Whitby et al. 2000; Busfield et al. 2004), and have ages consistent with the timing of metamorphism on the OC parent bodies, with the best interpretation of I-Xe ages around 4559 Ma (Busfield et al. 2004).

Various models have been proposed to account for the origin of halite and the source of water in the brines. One group of models assumes that halite formed on the H chondrite parent body: possible sources of water include exogenous water delivered to the parent body by cometary or asteroidal ice fragments (Zolensky et al. 1999; Bridges et al. 2004), dehydration of the asteroid interior (Whitby et al. 2000), and impact heating of phyllosilicates (Rubin et al. 2002). Bridges et al. (2004) argued that halite occurs as a clastic component of the breccia and did not precipitate in situ. More recent work has shown that halite contains a disequilibrium assemblage of diverse solid inclusions including silicates, phosphates, sulfides, oxides, macromolecular carbon, and light organic species (Fries et al. 2011; Zolensky et al. 2013). This assemblage is not obviously derived from an H chondrite parent body. Fries et al. (2011, 2013) suggest that halite could be derived from a carbonaceous asteroid, such as Ceres, or it could be

the product of cryovolcanism similar to what is observed on the Saturnian satellite Enceladus (Fries et al. 2011; Zolensky et al. 2013). Disequilibrium hydrogen and oxygen isotope ratios of fluid inclusions in halite indicate a D-rich and ^{16}O-poor source for the fluid, which is consistent with an origin on a carbonaceous parent body that had mixed with cometary water (Yurimoto et al. 2014). The presence of organic inclusions, as well as studies of the aqueous fluid inclusions in halite (Zolensky et al. 1999), provide strong evidence that halite has not been heated above 25 °C (Zolensky et al. 2013).

The predominance of halite in dark matrix and the highly Cl-rich compositions of apatite in matrix suggest that there may be a relationship between the two minerals and that their formation mechanisms could be coupled. In addition, the high apatite / merrillite ratio suggests a high fluid / rock ratio, since the overall abundance of phosphates is not unusually high (Table 1). Fluids would need to have a high Cl/F ratio, and the very low H_2O contents of apatite (Table 4) would also require such a fluid to be extremely H_2O-poor. Such a briny fluid might also precipitate halite: this could be a mechanism for an indigenous origin for halite. If halite is exogenous, one could argue that the halogens required to reset apatite compositions are delivered by the same mechanism as the halite, and that some of the impact material that included halite might vaporize and release Cl-rich fluids. An alternative model is that the presence of clastic halite (either indigenous or exogenous) contributed to secondary production of localized Cl-rich fluids: halite in Zag (and Monahans) contains fluid-filled fractures, providing evidence for fracturing and healing, most likely as a result of micrometeorite impacts in the regolith (Zolensky et al. 1999; Rubin et al. 2002), and this could have released Cl-rich fluids. If apatite compositions and the presence of halite are coupled, we might also expect halite to occur in H6-2 material. Unfortunately, we do not know if this is the case, since the thin section was not

528 prepared in water-absent conditions, and any halite present would have been lost in sample
529 preparation. The Cl-rich apatite compositions in H6-2 could mean that the H6-2 clast was
530 emplaced within matrix before H6-1, at the time when Cl-rich fluids were active.

531 The chlorine isotopic composition of halite in Zag is significantly lighter than that in
532 typical ordinary chondrite material, $\delta^{37}Cl \sim -2‰$ (Bridges et al. 2004; also, water-soluble
533 chloride analysis in Zag from Sharp et al. 2013), vs. a mean bulk value of -0.4 ‰ for all ordinary
534 chondrites (Sharp et al. 2013). Since little isotopic fractionation would be expected between
535 halite and the brine from which it precipitates, the brine must have been isotopically light.
536 Bridges et al. (2004) suggested that isotopic fractionation producing an isotopically light fluid
537 was unlikely to be a parent body process, and that the isotopically light fluid represents a
538 separate isotopic reservoir in the early solar system. Alternatively, we propose that an
539 isotopically light fluid could have formed as a result of degassing of metal chlorides in an H-
540 poor system, the counterpart of the analogous process that led to high $^{37}Cl/^{35}Cl$ ratios measured
541 in Apollo samples which were attributed to Cl degassing of anhydrous magmas (Sharp et al.
542 2010). Sharp et al. (2013) also observed isotopically light chlorine in the LL3.6 chondrite
543 Parnallee, in both the water-soluble fraction ($\delta^{37}Cl = -2.65‰$), and the structurally-bound
544 chloride component (mean $\delta^{37}Cl = -4.1‰$, indicating that a mechanism for producing
545 isotopically light chlorine must be reproducible, although uncommon, on ordinary chondrite
546 parent bodies.

547 We also need to consider the source of the more F-rich apatite compositions of H6-1.
548 One might argue that Cl-rich apatite compositions represent the final stages of evolution of a
549 halogen-rich fluid that was initially F-bearing, which evolved to more Cl-rich compositions due
550 to the relative partitioning behavior of F and Cl between apatite and fluid or melt (Boyce et al.

2014; McCubbin et al. 2015), in a process of fractional precipitation (similar to fractional crystallization). For example, halogen-bearing fluids may have been derived from the interior of the H chondrite parent body, either as a result of solid-state breakdown of halogen-bearing phases such as chondrule mesostasis at high metamorphic temperatures, or possibly as a result of degassing of a partial melt in the interior of the body (Elkins-Tanton et al. 2011; Weiss et al 2012). The latter mechanism would be consistent with light chlorine isotopes, if the fluid was H-poor. As the fluid migrated towards the asteroid surface, it would have interacted with merrillite or apatite already present in petrologic type 6 material, producing fluor-chlor-apatites (F-Cl-apatites). Apatite / merrillite intergrowth textures such as those illustrated in Fig. 9d,f are similar to textures in the unique primitive achondrite GRA 06128/06129 which are interpreted as replacement reactions that occurred when halogen-rich fluids interacted with previously existing merrillite grains (Shearer et al. 2011). Since F partitions strongly into apatite (Boyce et al. 2014; McCubbin et al. 2015), the fluid would become progressively depleted in F and enriched in Cl as it migrated through the parent body, resulting in more Cl-rich apatite compositions at lower depths (petrologic type 4). Extreme enrichment in Na and Cl could lead to precipitation of halite in the final stages. Further insight into this model would be gained by a better understanding of the relationship between F and H_2O contents, as well as D/H ratios, in apatite. A complication for this scenario is that apatite in the H6-2 clast is Cl-rich, not F-rich, so we cannot simply consider the parent body to have an onion-shell structure in which all H6 material records alteration by the same fluid. The parent body must have already been brecciated when fluid evolution occurred, i.e. the parent body would have had a rubble-pile structure, with H6-1 material located towards the centre and H4 and H6-2 material located closer to the surface.

573 If halite is exogenous, a relationship between apatite and halite is not required. An
574 alternative model for the formation of F-Cl-apatite is that it represents interactions with an F-
575 bearing fluid generated from localized, impact-related shock melting. Features that appear to be
576 impact melt veins and pockets occur in H6-1 material (Fig. 10), as well as chromite-plagioclase
577 assemblages (Fig. 10b) which are interpreted as being produced by shock (Rubin 2003). Rubin et
578 al. (2002) also describe shock features in H6 material in Zag. We suggest that impact melts could
579 have degassed volatiles, including F, and that the F-bearing vapor derived from such an event
580 either interacted with pre-existing apatite or precipitated apatite, resulting in heterogeneous
581 apatite compositions. F-Cl-apatite compositions would form initially, followed by Cl-rich apatite
582 as the F inventory of the fluid is rapidly depleted due to the relative partitioning behavior of F
583 relative to Cl between apatite and fluid. Alternatively, F-Cl-apatite could have precipitated
584 from an impact melt that had degassed Cl. Further support for an impact-related scenario is that
585 F-Cl-apatite is also observed in the L4 host of the L chondrite regolith breccia, Kendleton (Lewis
586 and Jones 2016), suggesting that F-bearing fluids might be more generally associated with
587 regolith breccias and surface processingSince heterogeneous Cl/F ratios of apatite would become
588 homogenized by diffusion over metamorphic timescales (see Jones et al. 2014), continuous
589 impact processing would need to extend into the time period when the asteroid was cooling.

590 Although we cannot argue for a unique scenario to explain the apatite compositions in
591 Zag, it is clear that formation conditions of apatites in different lithologies must have been
592 locally controlled, which in turn means that compositions were set prior to assembly of the
593 material we now observe as the Zag brecciated chondrite. Our preferred interpretation of the
594 complex nature of this rock is as follows. Merrillite and apatite were formed initially in a similar
595 way to unbrecciated chondrites, at varying depths in the H chondrite parent body. Repeated

596 impacts resulted in brecciation and regolith formation, mixing clasts of different lithologies at
597 the asteroid surface. Impacts into this material produced F-bearing, Cl-rich and H_2O-poor fluids,
598 and fractional precipitation of these fluids led to formation of F-Cl-apatite, followed by Cl-rich
599 apatite, and finally halite. In this scenario, both apatite and halite are retrograde phases that form
600 during cooling, and halite forms at the lowest temperatures. This model argues against the
601 interpretation that halite is exogenous. We suggest that the mélange of solid inclusions found in
602 halite (Fries et al. 2011, Zolensky et al. 2013) may represent fine-grained detritus at the surface
603 of the H asteroid, derived from regolith formation as well as bombardment by interplanetary dust
604 and micrometeorites. The D-rich and ^{16}O-poor cometary signature of the fluid inclusions in
605 halite (Yurimoto et al. 2014) could be derived from a cometary impactor, as proposed by
606 Zolensky et al. (1999) and Bridges et al. (2004). Further clarification of the behavior of halogens
607 in Zag will need detailed observations of a range of lithologies in multiple thin sections, to
608 investigate relationships between apatite compositions, the presence of halite, and host
609 petrography in more detail.

610 **Implications**

611

612 The factors affecting the formation and evolution of apatite in ordinary chondrites are
613 varied and complex, but unraveling them can potentially help to interpret the complex behavior
614 of fluids on the asteroids that represent chondritic parent bodies. Compositions of apatites are
615 heterogeneous on a scale of individual chondrites from the same chondrite group, and on a scale
616 of individual lithologies within brecciated chondrites, indicating that fluid compositions are
617 highly localized and that fluids were active as the asteroids cooled. This observation is an
618 important consideration for understanding the internal structure of chondritic asteroids, with

implications for physical as well as mechanical properties of the bulk asteroid. The suggestion that F-Cl-apatites may be associated with regolith breccias could have important broader implications: if halogens are readily degassed from impact-melt materials close to an asteroid surface, significant volatile loss could have occurred, even on chondritic asteroids. For an asteroid that underwent extensive melting, such as the parent body of an achondrite, volatile loss would have been considerable. The volatile inventories of terrestrial planets are probably considerably more depleted than the CI carbonaceous chondrite abundances that are commonly assumed.

Acknowledgements

We wish to thank reviewers S. Itoh and A. Rubin for useful comments, Michael Spilde forassistance with electron microprobe analyses, and Jonathan Lewis for helpful discussions. Electron microprobe and SEM work was carried out in the Electron Microbeam Analysis Facility, Department of Earth and Planetary Sciences and Institute of Meteoritics, University of New Mexico. The work was partially funded by NASA grant NNX12AH61G (P.I. R. Jones). FMM acknowledges support from the NASA Cosmochemistry Program through grant NNX14AK43G (P.I. FMM).

641 **References**

642

643 Bogard, D.D., Garrison, D.H., and Masarik, J. (2001) The Monahans chondrite and halite: Ar-
644 gon-39/argon-40 age, solar gases, cosmic-ray exposure ages, and parent body regolith neutron
645 flux thickness. Meteoritics and Planetary Science, 36, 107–122.

646 Boyce, J.W., Tomlinson, S.M., McCubbin, F.M., Greenwood, J.P., and Treiman, A.H. (2014)
647 The lunar apatite paradox. Science, 344, 400-402.

648 Brearley, A.J., and Jones, R.H. (1998) Chondritic meteorites. In J.J. Papike, Ed., Planetary Mate-
649 rials, 36, p. 3-1 to 3-398. Reviews in Mineralogy, Mineralogical Society of America, Chantilly,
650 Virgina.

651 Brearley, A.J., and Jones, R.H. (2016) Halogens in chondritic meteorites. In D. Harlov, Ed., The
652 Role of Halogens in Terrestrial and Extraterrestrial Geochemical Processes. Springer. (In
653 revision.)

654 Bridges, J.C., and Hutchison, R. (1997) A survey of clasts and large chondrules in ordinary
655 chondrites. Meteoritics and Planetary Science, 32, 389–394.

656 Bridges, J.C., Banks, D.A., Smith, M., and Grady, M.M. (2004) Halite and stable chlorine iso-
657 topes in the Zag H3-6 breccia. Meteoritics and Planetary Science, 39, 657-666.

658 Busfield, A.; Gilmour, J.D.; Whitby, J.A.; and Turner, G. (2004) Iodine-xenon analysis of ordi-
659 nary chondrite halide: implications for early solar system water. Geochimica et Cosmochimica
660 Acta, 68, 195-202.

661 Elkins-Tanton, L.T., Weiss, B.P., and Zuber, M.T. (2011) Chondrites as samples of differentiat-
662 ed planetesimals. Earth and Planetary Science Letters, 305, 1–10.

663 Fodor, R.R., Keil, K., Jarosewich, E., and Huss, G.I. (1972) The Oro Grande, New Mexico,
664 chondrite and its lithic inclusions Meteoritics, 7, 495-507.

665 Folco, L., Mellini, M., and Pillinger, C.T. (1996) Unshocked equilibrated H-chondrites: A
666 common low-temperature record from orthopyroxene iron-magnesium ordering. Meteoritics and
667 Planetary Science, 31, 388-393.

668 Fries, M., Zolensky, M., and Steele, A. (2011) Mineral inclusions in Monahans and Zag halites:
669 Evidence of the originating body. 74th Annual Meeting of the Meteoritical Society, Abstract
670 5390.

671 Fries, M., Messenger, S., Steele, A., and Zolensky, M. (2013) Do we already have samples of
672 Ceres? H chondrite halites and the Ceres-Hebe link. 76th Annual Meeting of the Meteoritical
673 Society, Abstract 5266.

674 Grossman, J.N. (1999) The Meteoritical Bulletin, No. 83, 1999 July. Meteoritics and Planetary
675 Science, 34, 169-186.

676 Huss, G.R., Rubin, A.E., and Grossman, J.N. (2006) Thermal metamorphism in chondrites. In
677 Meteorites and the Early Solar System II (eds. D.S. Lauretta and H.Y. McSween, Jr.) The Uni-
678 versity of Arizona Press, Tucson, AZ. pp. 597-586.

679 Hutchison, R., Williams, C.T., Din, V.K., Clayton, R.N., Kirschbaum, C., Paul, R.L., and
680 Lipschutz, M.E. (1988). A planetary, H-group pebble in the Barwell, L6, unshocked chondritic
681 meteorite. Earth and Planetary Science Letters, 90, 105–118.

682 Jones, R.H. (2007) A metamorphosed igneous inclusion in the Oro Grande H5 ordinary
683 chondrite. 70th Annual Meeting of the Meteoritical Society, Abstract #5213.

Jones, R.H., and Brearley, A.J. (2010a) Late-stage fluids on the LL chondrite parent body: Evidence from feldspar in the LL4 chondrites Bo Xian and Bjurböle. Lunar Planet Sci. XLI. Lunar and Planetary Science Institute, Houston, Abstract #2133.

Jones, R.H., and Brearley, A.J. (2010b) Fluids on the LL chondrite parent body: Evidence from the Bo Xian chondrite. Meteoritics and Planetary Science Supplement 45, Abstract #5276.

Jones, R.H., McCubbin, F.M., Dreeland, L., Guan, Y., Burger, P.V., and Shearer, C.K. (2014) Phosphate minerals in LL chondrites: A record of the action of fluids during metamorphism on ordinary chondrite parent bodies. Geochimica et Cosmochimica Acta, 132, 120-140.

Kovach, H.A., and Jones, R.H. (2010) Feldspar in type 4-6 ordinary chondrites: A record of metamorphic processing on the H and LL chondrite parent bodies. Meteoritics and Planetary Science, 45, 246–264.

Lewis, J.A., and Jones, R.H. (2014) Microtextural study of feldspar in petrologic type 3 LL ordinary chondrites: A record of parent body metasomatism. 77th Annual Meeting of the Meteoritical Society, Abstract #5176.

Lewis, J.A., and Jones, R.H. (2015) Microtextural study of feldspar in petrologic type 4 ordinary chondrites: Contrasting records of parent body metasomatism. 78th Annual Meeting of the Meteoritical Society, Abstract #5119.

Lewis, J.A., and Jones, R.H. (2016) Phosphate and feldspar mineralogy of equilibrated L chondrites: The record of metasomatism during metamorphism in ordinary chondrite parent bodies. Meteoritics and Planetary Science, in press.

McCubbin, F.M., and Jones, R.H. (2015) Extraterrestrial apatite: Planetary geochemistry to astrobiology. Elements, 11, 183-188.

McCubbin, F.M., Steele, A., Nekvasil, H., Schnieders, A., Rose, T., Fries, M., Carpenter, P.K., and Jolliff, B.L. (2010a) Detection of structurally bound hydroxyl in fluorapatite from Apollo mare basalt 15058, 128 using TOF-SIMS. American Mineralogist, 95, 1141–1150.

McCubbin, F.M., Steele, A., Hauri, E.H., Nekvasil, H., Yamashita, S., and Hemley, R.J. (2010b) Nominally hydrous magmatism on the Moon. Proceedings of the National Academy of Sciences USA, 27, 11223–11228.

McCubbin, F.M., Jolliff, B.L., Nekvasil, H., Carpenter, P.K., Zeigler, R.A., Steele, A., Elardo, S.M., and Lindsley, D.H. (2011) Fluorine and chlorine abundances in lunar apatite: Implications for heterogeneous distributions of magmatic volatiles in the lunar interior. Geochimica et Cosmochimica Acta, 75, 5073–5093.

McCubbin, F.M., Hauri, E.H., Elardo, S.M., Vander Kaaden, K.E., and Wang, J. (2012) Hydrous melting of the Martian mantle produced both depleted and enriched shergottites. Geology, 40, 683-686.

McCubbin, F.M., Elardo, S.M., Shearer, C.K., Smirnov, A., Hauri, E.H., and Draper, D.S. (2013) A petrogenetic model for the co-magmatic origin of chassignites and nakhlites: Inferences from chlorine-rich minerals, petrology, and geochemistry. Meteoritics and Planetary Science, 48, 819-853.

McCubbin, F.M., Vander Kaaden, K.E., Tartèse, R., Boyce, J.W., Mikhail, S., Whitson, E.S., Bell, A.S., Anand, M., Franchi, I.A., Wang, J.H., and Hauri, E.H. (2015) Experimental investigation of F, Cl, and OH partitioning between apatite and Fe-rich basaltic melt at 1.0-1.2 GPa and 950-1000 ^{o}C. American Mineralogist, 100, 1790-1802.

Rubin, A.E. (1994) Metallic copper in ordinary chondrites. Meteoritics, 29, 93-98.

728 Rubin, A.E. (2003) Chromite-plagioclase assemblages as a new shock indicator; Implications for
729 the shock and thermal histories of ordinary chondrites. Geochimica et Cosmochimica Acta, 67,
730 2695–2709.

731 Rubin, A.E. (2004) Postshock annealing and postannealing shock in equilibrated ordinary
732 chondrites: implications for the thermal and shock histories of chondritic asteroids. Geochimica
733 et Cosmochimica Acta, 68, 673–689.

734 Rubin, A.E., and Grossman J.N. (1985) Phosphate-sulfide assemblages and Al/Ca ratios in type-
735 3 chondrites. Meteoritics, 20, 479-489.

736

737 Rubin, A.E., Zolensky, M.E., and Bodnar, R.J. (2002) The halite-bearing Zag and Monahans
738 (1998) meteorite breccias: Shock metamorphism, thermal metamorphism and aqueous alteration
739 on the H-chondrite parent body. Meteoritics and Planetary Science, 37, 125-141.

740 Rubin, A.E., Ziegler K., and Young E.D. (2008) Size scales over which ordinary chondrites and
741 their parent asteroids are homogeneous in oxidation state and oxygen-isotopic composi-
742 tion. Geochimica et Cosmochimica Acta 72, 948-958.

743 Ruzicka, A., Snyder, G.A., and Taylor, L.A. (1998) Megachondrules and large, igneous-textured
744 clasts in Julesberg (L3) and other ordinary chondrites: Vapor-fractionation, shock-melting, and
745 chondrule formation. Geochimica et Cosmochimica Acta, 62,1419–1442.

746 Ruzicka, A., Snyder, G.A., and Taylor, L.A. (2000) Geochemical and isotopic evidence bearing
747 on the origin of large, igneous-textured inclusions in ordinary chondrites. Antarctic Meteorite
748 Research, 13, 19–38.

749 Ruzicka, A., Hutson, M., Floss, C., and Hildebrand, A. (2012) Large silica-rich igneous-textured
750 inclusions in the Buzzard Coulee chondrite: Condensates, differentiates, or impact melts?
751 Meteoritics and Planetary Science, 47, 1809-1829.

752 Schneider, C.A., Rasband, W.S., and Eliceiri, K.W. (2012) "NIH Image to ImageJ: 25 years of
753 image analysis". Nature Methods, 9, 671-675.

754 Sharp, Z.D., Shearer, C.K., McKeegan, K.D., Barnes, J.D., and Wang, Y.Q. (2010) The chlorine
755 isotope composition of the Moon and implications for an anhydrous mantle. Science, 329, 1050–
756 1053.

757 Sharp, Z.D., Mercer, J.A., Jones, R.H., Brearley, A.J., Selverstone, J., Bekker, A., and
758 Stachel, T. (2013) The chlorine isotope composition of chondrites and Earth. Geochimica et
759 Cosmochimica Acta, 107, 189-204.

760 Shearer, C.K., Burger, P.V., Papike, J.J., Sharp, Z.D., and McKeegan, K.D. (2011) Fluids on dif-
761 ferentiated asteroids: Evidence from phosphates in differentiated meteorites GRA 06128 and
762 GRA 06129. Meteoritics and Planetary Science, 46, 1345–1362.

763 Stöffler, D., Keil, K., and Scott, E.R.D. (1991) Shock metamorphism of ordinary chondrites.
764 Geochimica et Cosmochimica Acta, 55, 3845-3867.

765 Stormer, J.C.Jr., Pierson, M.J., and Tacker, R.C. (1993) Variation of F and Cl X-ray intensity
766 due to anisotropic diffusion of apatite during electron microprobe analysis. American Mineralo-
767 gist, 78, 641-648.

768 Van Schmus, W.R., and Wood, J.A. (1967) A chemical-petrological classification for the
769 chondritic meteorites. Geochimica et Cosmochimica Acta, 31, 747-765.

770 Weiss, B.P., Elkins-Tanton, L.T., Antonietta Barucci, M., Sierks, H., Snodgrass, C., Vincent, J-
771 B., Marchi, S., Weissman, P.R., Pätzold, M., Richter, I., Fulchignoni, M., Binzel, R.P., and
772 Schulz, R. (2012) Possible evidence for partial differentiation of asteroid Lutetia from Rosetta.
773 Planetary and Space Science, 66, 137-146.

774 Whitby, J., Burgess, R., Turner, G., and Gilmour, J. (2000) Extinct ^{129}I in Halite from a Primitive
775 Meteorite: Evidence for Evaporite Formation in the Early Solar System. Science, 288, 1819-
776 1821.

777 Yurimoto, H., Itoh, S, Zolensky, M.E., Kusakabe, M., Karens, A., and Bodnar, R. (2014) Isotop-
778 ic compositions of asteroidal liquid water trapped in fluid inclusions of chondrites. Geochemical
779 Journal, 48, 549-560.

780 Zanda, B., Bourot-Denise, M., Perron, C., and Hewins, R.H. (1994) Origin and metamorphic re-
781 distribution of silicon, chromium, and phosphorus in the metal of chondrites. Science, 265, 1846-
782 1849.

783 Zolensky, M.E., Bodnar, R.J., Gibson, E.K.Jr., Nyquist, L.E., Reese, Y., Shih, C-Y., and
784 Wiesmann, H. (1999) Asteroidal water within fluid inclusion-bearing halite in an H5 chondrite,
785 Monahans (1998). Science, 285, 1377-1379.

786 Zolensky, M.E., Fries, M., Bodnar, R., Yurimoto, H., Itoh, S., Steele, A., Mikouchi, T.,
787 Hagiya, K., Ohsumi, K., Le, L., and Rahman, Z. (2013) Early solar system cryovolcanics in the
788 laboratory. 76th Annual Meeting of the Meteoritical Society, Abstract #5200.

789

790

This is a preprint, the final version is subject to change, of the American Mineralogist (MSA)
Cite as Authors (Year) Title. American Mineralogist, in press.
(DOI will not work until issue is live.) DOI: http://dx.doi.org/10.2138/am-2016-5728

791

Tables

Table 1: Modal abundances of phosphate minerals

Chondrite	Pet type	Shock stage[1]	Area mm^2	% Phosphate Minerals			
				Apatite	Merrillite	Total	Ap/Merr
Avanhandava	H4	S2	64	0.17	0.24	0.41	0.72
Oro Grande	H5	S1	96	0.21	0.29	0.50	0.72
Richardton	H5	S2	64	0.28	0.18	0.46	1.49
Estacado	H6	S1	73.5	0.15	0.38	0.52	0.39
Zag matrix	H4	S2-S5	67.5	0.23	0.05	0.28	4.60
Zag clast H6-1	H6	S2-S5	60.5	0.09	0.55	0.64	0.16

[1]Shock stages from Stöffler et al. (1991); Rubin (1994, 2004); Folco et al. (1996); Grossman (1999); Rubin et al. (2002)

792

793

794

795

796

797

798

799

Table 2: Average compositions of merrillite in H chondrites (EPMA data)

	Avan.	*1-sig*	Rich.	*1-sig*	Oro Gr.	*1-sig*	Est.	*1-sig*	Zag H6-1	*1-sig*	Zag H6-2
CaO	47.1	*0.2*	47.1	*0.2*	47.1	*0.1*	46.9	*0.3*	46.8	*0.5*	46.3
MgO	3.7	*0.1*	3.7	*0.0*	3.7	*0.0*	3.5	*0.0*	3.5	*0.0*	3.5
FeO	0.4	*0.1*	0.5	*0.2*	0.4	*0.1*	0.5	*0.3*	0.5	*0.2*	0.3
Na_2O	2.8	*0.0*	2.8	*0.0*	2.7	*0.0*	2.8	*0.0*	2.7	*0.1*	2.8
P_2O_5	45.5	*0.2*	45.3	*0.3*	45.1	*0.3*	45.6	*0.4*	46.0	*0.4*	45.3
Total	99.5		99.3		99.0		99.3		99.6	*0.7*	98.2
					Merrillite formula on the basis of 56 oxygens						
Ca	18.2	*0.1*	18.2	*0.1*	18.3	*0.1*	18.1	*0.1*	18.0	*0.1*	18.1
Mg	2.0	*0.0*	2.0	*0.0*	2.0	*0.0*	1.9	*0.0*	1.9	*0.0*	1.9
Fe	0.1	*0.0*	0.1	*0.1*	0.1	*0.0*	0.2	*0.1*	0.2	*0.1*	0.1
Na	1.9	*0.0*	2.0	*0.0*	1.9	*0.0*	1.9	*0.0*	1.9	*0.1*	1.9
P	13.9	*0.0*	13.9	*0.0*	13.8	*0.0*	13.9	*0.0*	14.0	*0.0*	14.0
Total	36.1	*0.1*	36.2	*0.1*	36.2	*0.1*	36.1	*0.1*	35.9	*0.1*	36.0
mg#	0.94		0.94		0.94		0.93		0.93		0.96
n	15		19		20		28		41		1

Avan: Avanhandava; Rich: Richardton; Oro Gr: Oro Grande; Est: Estacado
n = number of analyses
mg# = mg/(mg+fe)

800

801

802

803

Table 3: Apatite compositions in H chondrites (EPMA data)

	Avan.	*1-sig*	Rich.	*1-sig*	Oro Gr. host	*1-sig*	Oro Gr. inclusion	*1-sig*	Est.	*1-sig*	Zag H4	*1-sig*	Zag H6-1	*1-sig*	Zag H6-2	*1-sig*
CaO	53.5	*0.2*	53.1	*0.3*	53.7	*0.3*	53.6	*0.1*	53.6	*0.2*	52.3	*0.3*	53.4	*0.4*	52.5	*0.2*
MgO	0.05	*0.03*	0.05	*0.06*	0.09	*0.03*	0.06	*0.01*	0.05	*0.03*	0.10	*0.04*	0.05	*0.03*	0.09	*0.04*
FeO	0.44	*0.16*	0.27	*0.11*	0.41	*0.16*	0.28	*0.03*	0.18	*0.12*	0.61	*0.39*	0.47	*0.31*	0.38	*0.30*
Na_2O	0.35	*0.01*	0.42	*0.02*	0.31	*0.03*	0.35	*0.01*	0.43	*0.03*	0.50	*0.09*	0.27	*0.04*	0.48	*0.04*
P_2O_5	40.7	*0.2*	40.3	*0.2*	40.2	*0.4*	39.8	*0.2*	40.8	*0.3*	40.4	*0.2*	40.7	*0.3*	40.6	*0.3*
F	0.60	*0.07*	0.32	*0.11*	0.80	*0.11*	0.71	*0.08*	0.38	*0.12*	0.16	*0.08*	1.43	*0.34*	0.24	*0.18*
Cl	5.4	*0.1*	6.2	*0.2*	4.9	*0.2*	5.0	*0.1*	5.5	*0.2*	5.8	*0.2*	3.7	*0.5*	5.7	*0.4*
-O=F+Cl	1.5	*0.0*	1.5	*0.1*	1.5	*0.0*	1.4	*0.0*	1.4	*0.1*	1.4	*0.0*	1.4	*0.0*	1.4	*0.0*
Total	99.6	*0.4*	99.2	*0.3*	99.1	*0.4*	98.4	*0.2*	99.5	*0.4*	98.6	*0.6*	98.6	*0.5*	98.6	*0.5*
Cl/F (wt)	9.3	*1.2*	23.4	*14.3*	6.4	*1.1*	7.1	*0.9*	16.0	*5.9*	52.6	*45.4*	2.8	*1.2*	34.9	*18.8*
							Apatite formula on the basis of 13 anions									
Ca	4.97	*0.01*	4.98	*0.02*	5.01	*0.03*	5.04	*0.02*	4.97	*0.01*	4.91	*0.03*	4.96	*0.02*	4.91	*0.02*
Mg	0.01	*0.00*	0.01	*0.01*	0.01	*0.00*	0.01	*0.00*	0.01	*0.00*	0.01	*0.01*	0.01	*0.00*	0.01	*0.01*
Fe	0.03	*0.01*	0.02	*0.01*	0.03	*0.01*	0.02	*0.00*	0.01	*0.01*	0.04	*0.03*	0.03	*0.02*	0.03	*0.02*
Na	0.06	*0.00*	0.07	*0.00*	0.05	*0.01*	0.06	*0.00*	0.07	*0.01*	0.09	*0.01*	0.05	*0.01*	0.08	*0.01*
P	2.98	*0.01*	2.98	*0.01*	2.97	*0.01*	2.96	*0.01*	2.99	*0.01*	3.00	*0.01*	2.99	*0.01*	3.00	*0.01*
F	0.16	*0.02*	0.09	*0.03*	0.22	*0.03*	0.20	*0.02*	0.11	*0.03*	0.04	*0.02*	0.39	*0.09*	0.07	*0.05*
Cl	0.80	*0.02*	0.90	*0.02*	0.73	*0.03*	0.74	*0.01*	0.81	*0.03*	0.87	*0.03*	0.54	*0.08*	0.84	*0.06*
"Other" anion by diff	0.04	*0.02*	0.01	*0.02*	0.05	*0.02*	0.06	*0.01*	0.08	*0.04*	0.09	*0.02*	0.07	*0.02*	0.09	*0.02*
∑ Tetrahedral	2.98	*0.01*	2.98	*0.01*	2.97	*0.01*	2.96	*0.01*	2.99	*0.01*	3.00	*0.01*	2.99	*0.01*	3.00	*0.01*
∑ Octahedral	5.07	*0.01*	5.07	*0.02*	5.11	*0.03*	5.13	*0.02*	5.07	*0.02*	5.05	*0.02*	5.05	*0.03*	5.04	*0.01*
Cl/F (atomic)	5.0	*0.6*	12.4	*7.7*	3.4	*0.6*	3.8	*0.5*	8.6	*3.2*	28.2	*24.3*	1.5	*0.6*	18.7	*10.1*
Cl/(Cl+F) (atomic)	0.83	*0.02*	0.91	*0.03*	0.77	*0.03*	0.79	*0.02*	0.89	*0.03*	0.95	*0.02*	0.58	*0.09*	0.93	*0.06*
n	9		16		9		3		21		13		26		16	

Avan: Avanhandava; Rich: Richardton; Oro Gr: Oro Grande; Est: Estacado
n = number of analyses

804

805

806

807

808

809

810

Table 4: Volatile anion analyses of merrillite and apatite in Zag

Grain	Host material	H_2O, ppm SIMS[1]	S, ppm SIMS[1]	F, wt% SIMS[1]	F, wt% EPMA[2]
Apatite M2D	H6-2	599	97	0.11	0.10-0.28
Apatite P11	H4	358	117	0.05	0.13
Apatite P7	H6-1	439	154	1.58	1.05-1.78
Merrillite P1	H6-1	744	64	-0.08	0

[1]OH, S and F determined by SIMS based on calibrations from apatite standards

[2]F wt% measured directly by electron microprobe: ranges are for multiple analyses on a single grain

811

812 **Figure Captions**

813 Fig. 1. BSE images showing occurrences of phosphate minerals in Ahanhandava (H4): ap =
814 apatite, merr = merrillite. The silicate mineral assemblage in all images includes olivine (olv),
815 which is lighter grey than low-Ca pyroxene (pyx), and feldspar (dark grey – noticeable in
816 chondrule interiors in (c) and (d)). White phases include Fe,Ni metal and troilite (FeS). a) Fine-
817 grained assemblage of apatite and merrillite intergrown with pyroxene and metal; b) Fine-
818 grained apatite adjacent to metal; c,d) occurrence of merrillite at the margins of relict chondrules
819 (rounded objects).

820

821 Fig. 2. BSE images showing occurrences of phosphate minerals in Richardton (H5): ap = apatite,
822 merr = merrillite. The silicate mineral assemblage in all images includes olivine (olv), which is
823 lighter grey than low-Ca pyroxene (pyx), and feldspar (dark grey). White phases include Fe,Ni
824 metal and troilite (FeS). a) Apatite grain with inclusions of merrillite, olivine (dark grey) and
825 metal (white). Apatite also occurs in fine veins adjacent to the large grain. b) Fractured apatite
826 grain with an inclusion of merrillite. c) Individual grains of merrillite and apatite. Merrillite also
827 occurs in fine veins adjacent to the large grain. d) Individual grain of merrillite. In (b), (c), and
828 (d), phosphate grains are in contact with metal.

829

830 Fig. 3. BSE images showing occurrences of phosphate minerals in Estacado (H6): ap = apatite,
831 merr = merrillite. The silicate mineral assemblage in all images includes olivine (olv), which is
832 lighter grey than low-Ca pyroxene (pyx), and feldspar (dark grey). White phases include Fe,Ni
833 metal and troilite (FeS). Both phosphate minerals are distributed throughout the chondrite with

834 similar grain sizes and as mostly uniform individual grains. Fig. 3(d) shows merrillite and apatite
835 grains that appear to be associated with a chromite-plagioclase assemblage (CPA).
836
837 Fig. 4. BSE images showing occurrences of phosphate minerals in Oro Grande (H5): ap =
838 apatite, merr = merrillite. The silicate mineral assemblage in all images includes olivine (olv),
839 which is lighter grey than low-Ca pyroxene (pyx), and feldspar (dark grey). White phases
840 include Fe,Ni metal and troilite (FeS). White veins throughout the images are the product of
841 terrestrial weathering. Both phosphate minerals occur as individual grains as well as intergrown
842 together e.g. in (a), (c) and (d). Both phosphate minerals occur at the margins of the large (5 mm)
843 igneous inclusion which is visible in (c) and (d).
844
845 Fig. 5. Texture and occurrence of apatite (ap) in the 5 mm igneous inclusion in Oro Grande (H5).
846 a,b) BSE images showing large apatite grains surrounding features that appear to be fine-grained
847 pseudomorphs of phenocrysts in a porphyritic rock. The groundmass is a fine-grained mixture of
848 olivine (light grey) and feldspar (dark grey) with a barred texture. Small white grains are
849 predominantly chromite. c,d,e) X-ray maps of the area shown in (b), highlighting phenocrystic
850 texture. (e) Combined X-ray map, RGB = Mg,Na,Ca. Apatite shows as pink in the Ca map and
851 blue in the combined map. Olivine is pink in the Mg map and bright red in the combined map.
852 Albitic feldspar is green in the combined map. Low-Ca pyroxene is yellow in the Mg map and
853 dull red in the combined map. Diopside is light blue in the Mg and Ca maps and purple in the
854 combined maps.
855

856 Fig. 6. Anions in apatite in H chondrites. The apex of the ternary labeled "other" is usually
857 assigned to OH^-, but we prefer to label it "other" since there is little evidence for OH in
858 chondritic apatite (see text). a) Apatite compositions in non-brecciated chondrites. b) Apatite
859 compositions in the H3-6 breccia, Zag. Lithologies identified as H4 matrix, H6-1 and H6-2 are
860 identified in Fig. 7.
861
862 Fig. 7. Thin section of the Zag H3-6 chondrite studied. a) Optical scan of thin section UNM
863 1136: circular thin section is 2.5 cm in diameter. H4 matrix material is dark, and two H6 clasts,
864 H6-1 and H6-2, are light. The small box with solid outline is the region shown in (b) and the
865 larger box with dashed outline is the region shown in the X-ray maps, (c)-(f). Fine-dashed line
866 outlines the contact between H4 matrix and H6-1 regions. b) BSE image showing the contact
867 between regions H6-2 and H4 matrix, which is highlighted with a dashed line. The H6 lithology
868 is coarse-grained and contains coarse-grained metal and sulfide aggregates (white). Apatite (ap)
869 occurs as large individual grains (light grey) in both lithologies. c-f) X-ray maps showing
870 distributions of Fe, S, P and Cl in the region outlined in (a). Sulfide is fine-grained in H4 matrix
871 and coarser-grained in H6-1. Apatite is concentrated in the H4 matrix material (see Cl map) and
872 merrillite occurs in both matrix and H6-1 lithologies, but has significantly larger grain size in
873 H6-1.
874
875 Fig. 8. BSE images of phosphate grains in the H4 matrix of Zag: ap = apatite, me = merrillite.
876 The silicate mineral assemblage in all images includes feldspar, olivine, low-Ca pyroxene, and
877 Ca-rich pyroxene, in order of increasing grey-level. White grains include Fe,Ni metal and troilite
878 (FeS). a) Several irregular shaped apatite grains and a small merrillite grain associated with

879 metal (top). b) Several apatite grains and two small merrillite grains (center). Chondrules are
880 clearly defined. c) Apatite and small merrillite grains: elongate apatite in the center has a vein-
881 like extension from the right side of the grain.
882
883 Fig. 9. BSE images of phosphate grains in the H6 lithologies of Zag: ap = apatite, merr =
884 merrillite. The silicate mineral assemblage in all images includes olivine (olv), which is lighter
885 grey than low-Ca pyroxene (pyx), and feldspar (dark grey). White phases include Fe,Ni metal
886 and troilite (FeS). a) Individual merrillite grain in H6-1. b) Merrillite grains in H6-1 showing
887 lineations that appear to be crystallographically controlled. c) Apatite grains in H6-1 (d)
888 Intergrown apatite and merrillite in H6-1. (e) Apatite in an assemblage with chromite (chro) and
889 olivine (olv) in H6-1. (f) Large apatite grain with an inclusion of merrillite in H6-2.
890
891 Fig. 10. a) Region of Zag region H6-1 showing merrillite (light grey: red arrows) that appears to
892 occur in a sinuous feature interpreted as an annealed melt vein. The sinuous feature is defined by
893 plagioclase (plag: dark grey) and includes a chromite-plagioclase assemblage (CPA). b) Higher
894 magnification image of the chromite-plagioclase assemblage in (a), chro = chromite, plag =
895 plagioclase, merr = merrillite. c) Apatite and merrillite in H6-1. The lower part of the large
896 apatite grain appears to have undergone incipient melting into a feldspathic melt. d) Merrillite in
897 H6-1. A fine-grained equigranular region of low-Ca pyroxene (pyx), Ca-rich pyroxene (cpx) and
898 plagioclase contains fine-grained (<5 μm) merrillite distributed along grain boundaries.
899
900

This is a preprint, the final version is subject to change, of the American Mineralogist (MSA)
Cite as Authors (Year) Title. American Mineralogist, in press.
(DOI will not work until issue is live.) DOI: http://dx.doi.org/10.2138/am-2016-5728

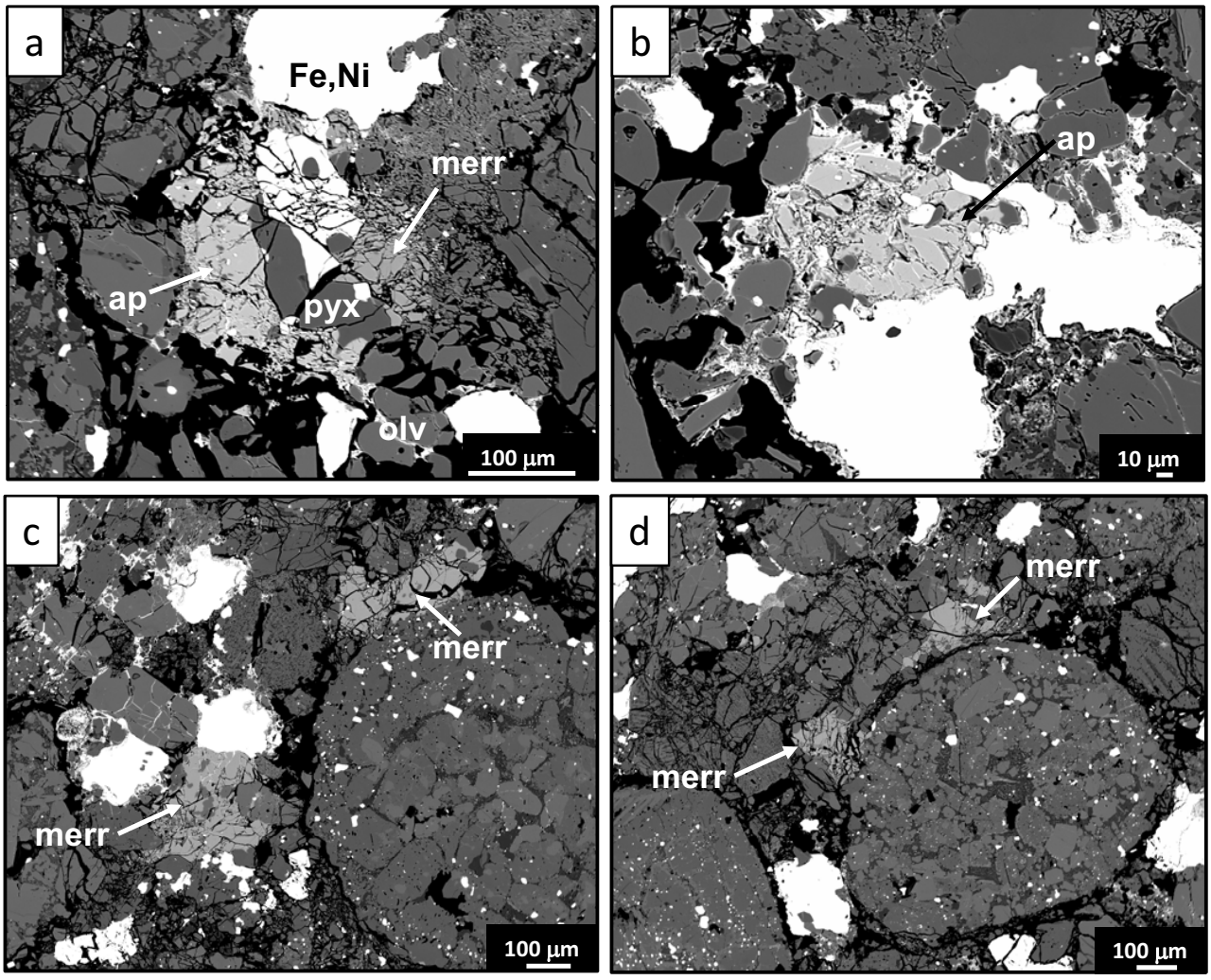

Fig. 1

Avanhandava

This is a preprint, the final version is subject to change, of the American Mineralogist (MSA)
Cite as Authors (Year) Title. American Mineralogist, in press.
(DOI will not work until issue is live.) DOI: http://dx.doi.org/10.2138/am-2016-5728

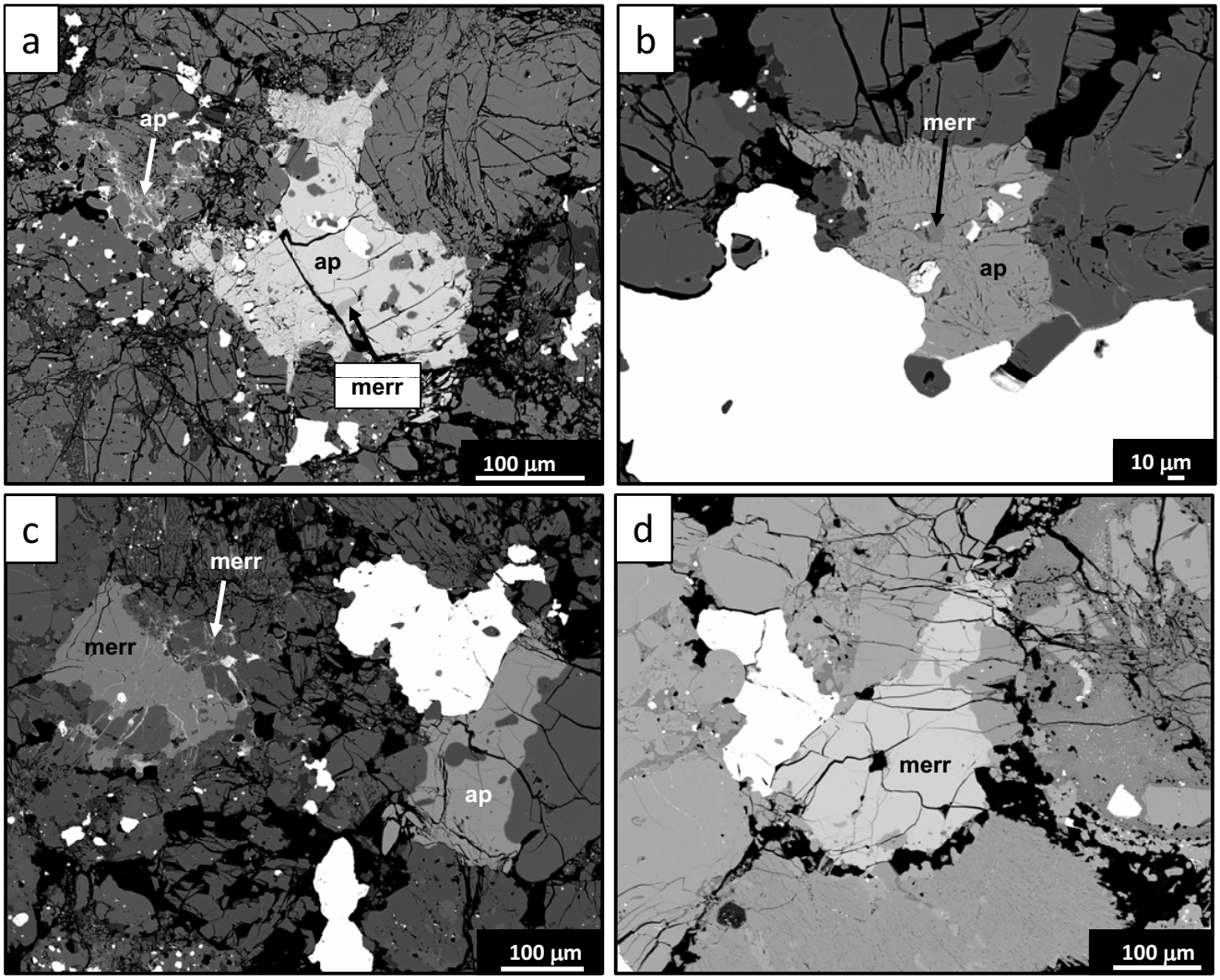

Fig. 2

Richardton

This is a preprint, the final version is subject to change, of the American Mineralogist (MSA)
Cite as Authors (Year) Title. American Mineralogist, in press.
(DOI will not work until issue is live.) DOI: http://dx.doi.org/10.2138/am-2016-5728

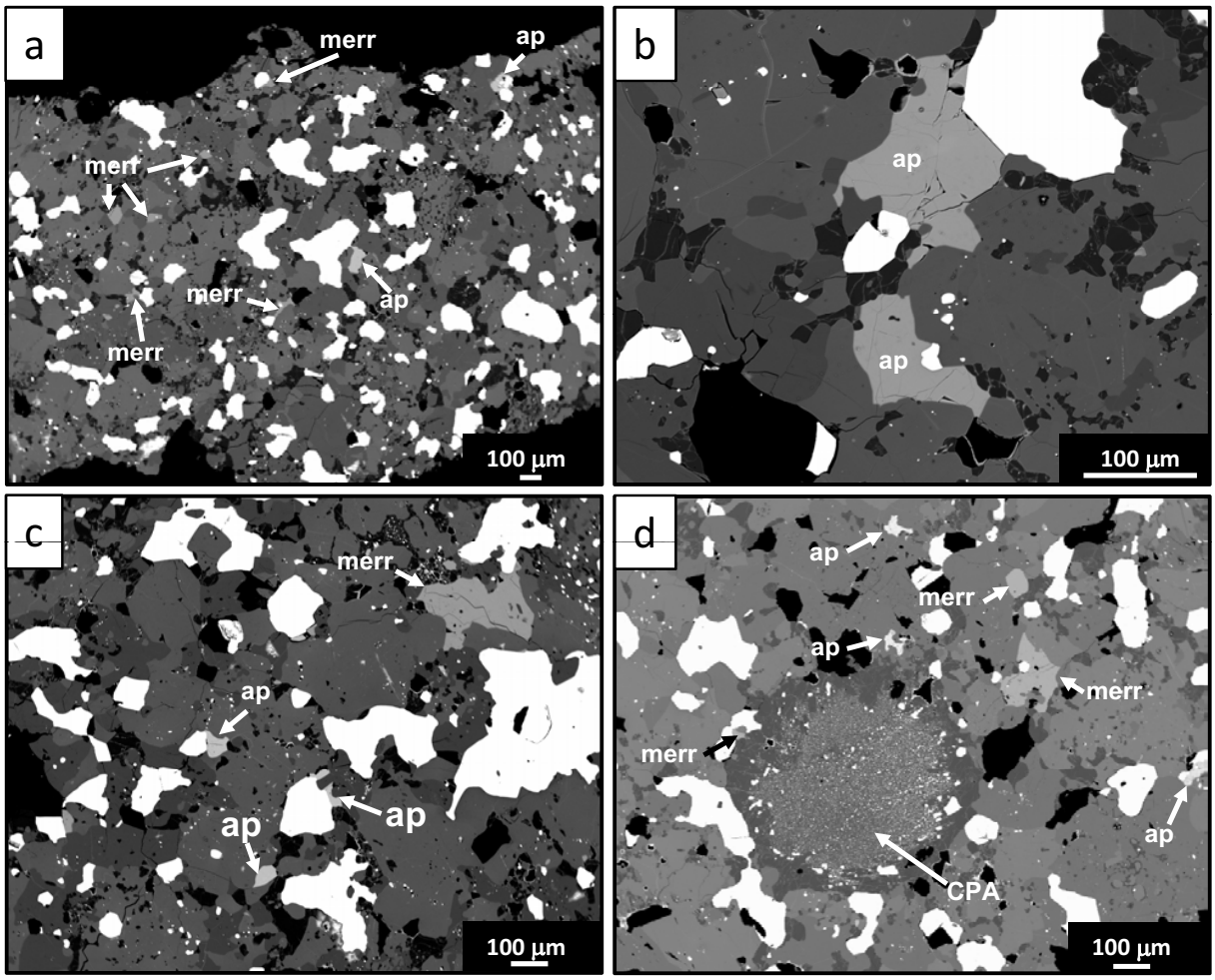

Fig. 3

Estacado

This is a preprint, the final version is subject to change, of the American Mineralogist (MSA)
Cite as Authors (Year) Title. American Mineralogist, in press.
(DOI will not work until issue is live.) DOI: http://dx.doi.org/10.2138/am-2016-5728

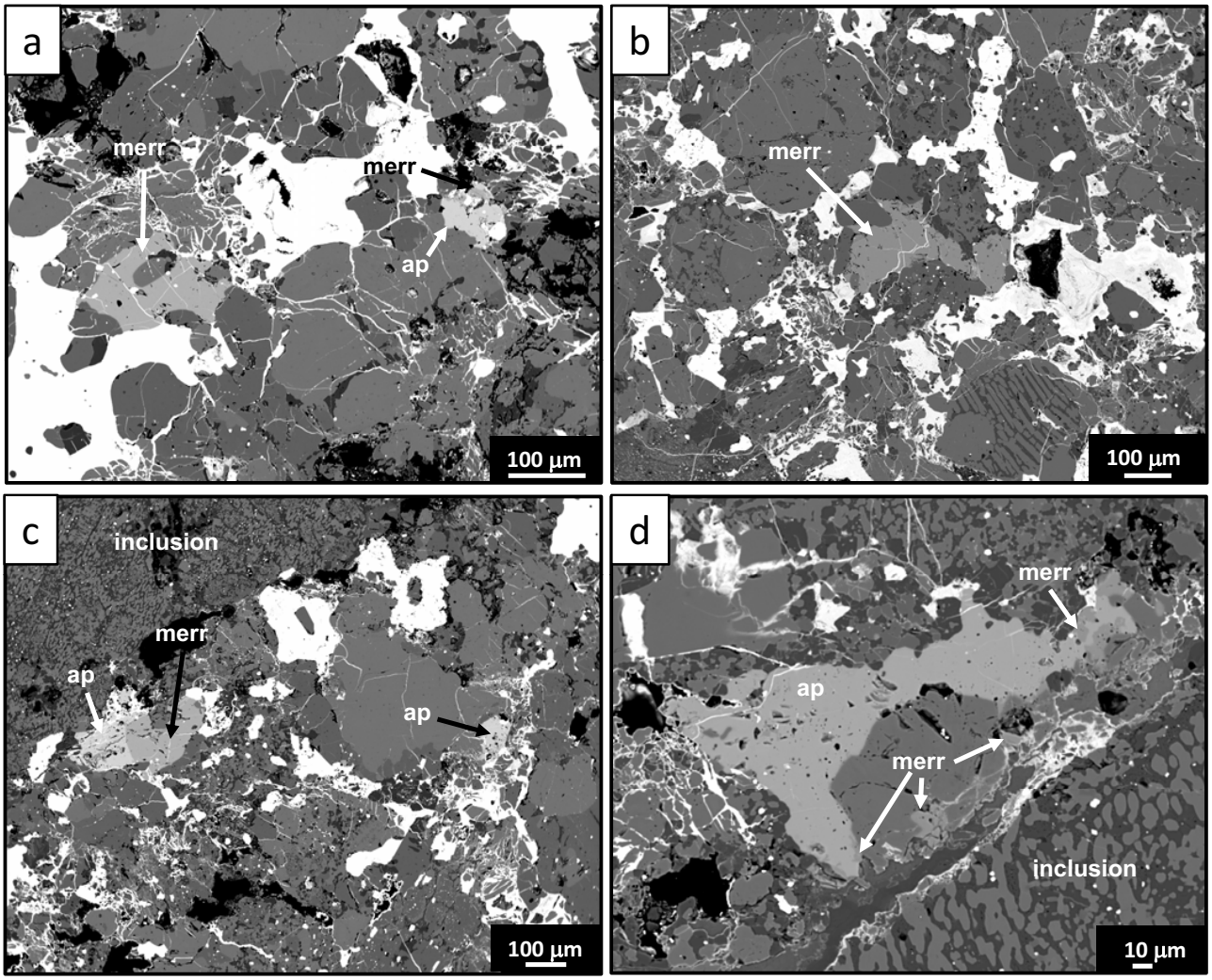

Fig. 4

Oro Grande

This is a preprint, the final version is subject to change, of the American Mineralogist (MSA)
Cite as Authors (Year) Title. American Mineralogist, in press.
(DOI will not work until issue is live.) DOI: http://dx.doi.org/10.2138/am-2016-5728

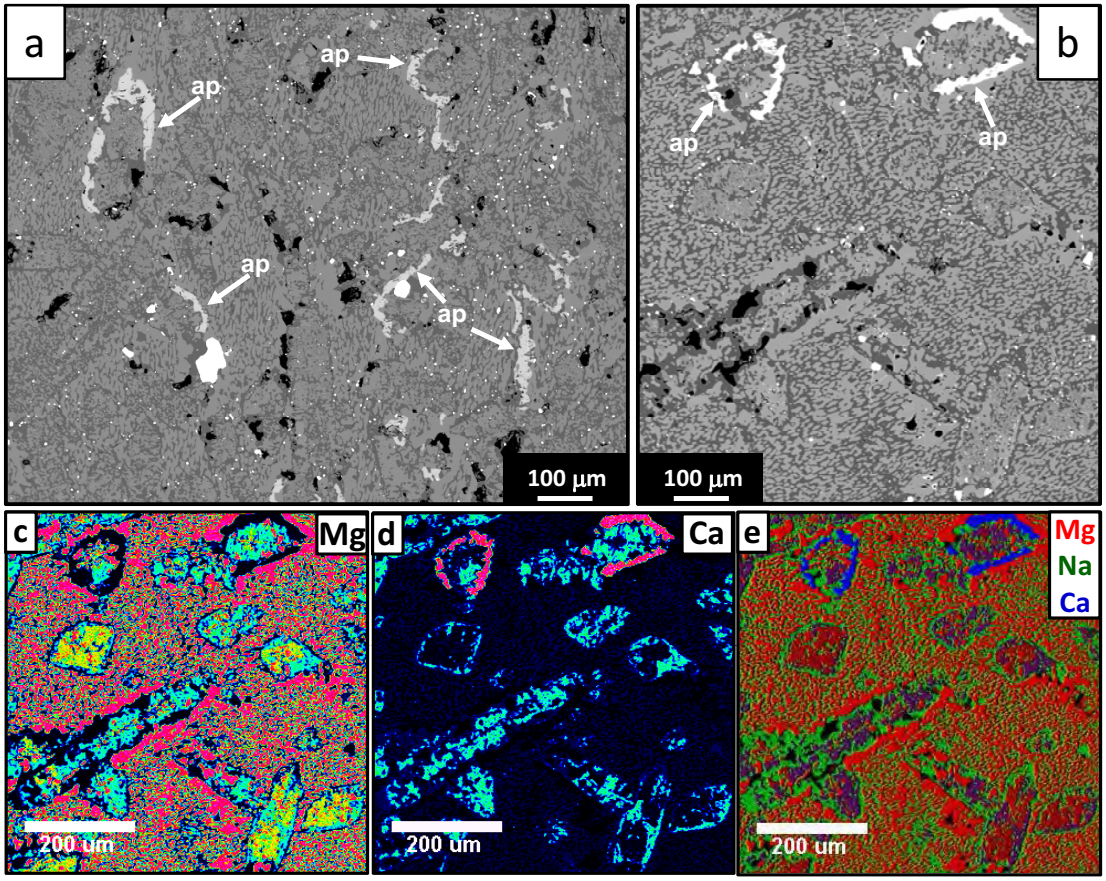

Fig. 5

Oro Grande Inclusion

This is a preprint, the final version is subject to change, of the American Mineralogist (MSA)
Cite as Authors (Year) Title. American Mineralogist, in press.
(DOI will not work until issue is live.) DOI: http://dx.doi.org/10.2138/am-2016-5728

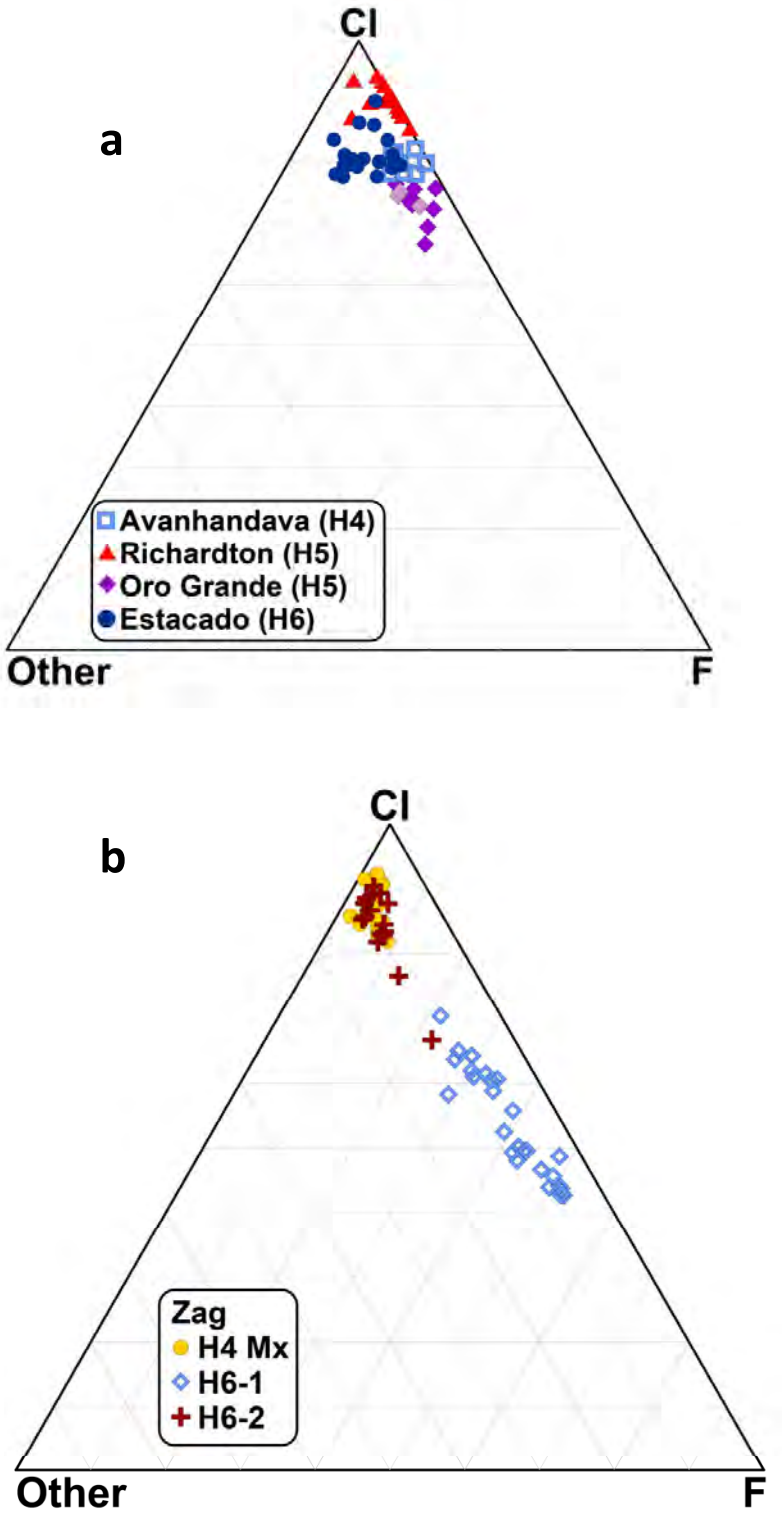

Fig. 6

This is a preprint, the final version is subject to change, of the American Mineralogist (MSA)
Cite as Authors (Year) Title. American Mineralogist, in press.
(DOI will not work until issue is live.) DOI: http://dx.doi.org/10.2138/am-2016-5728

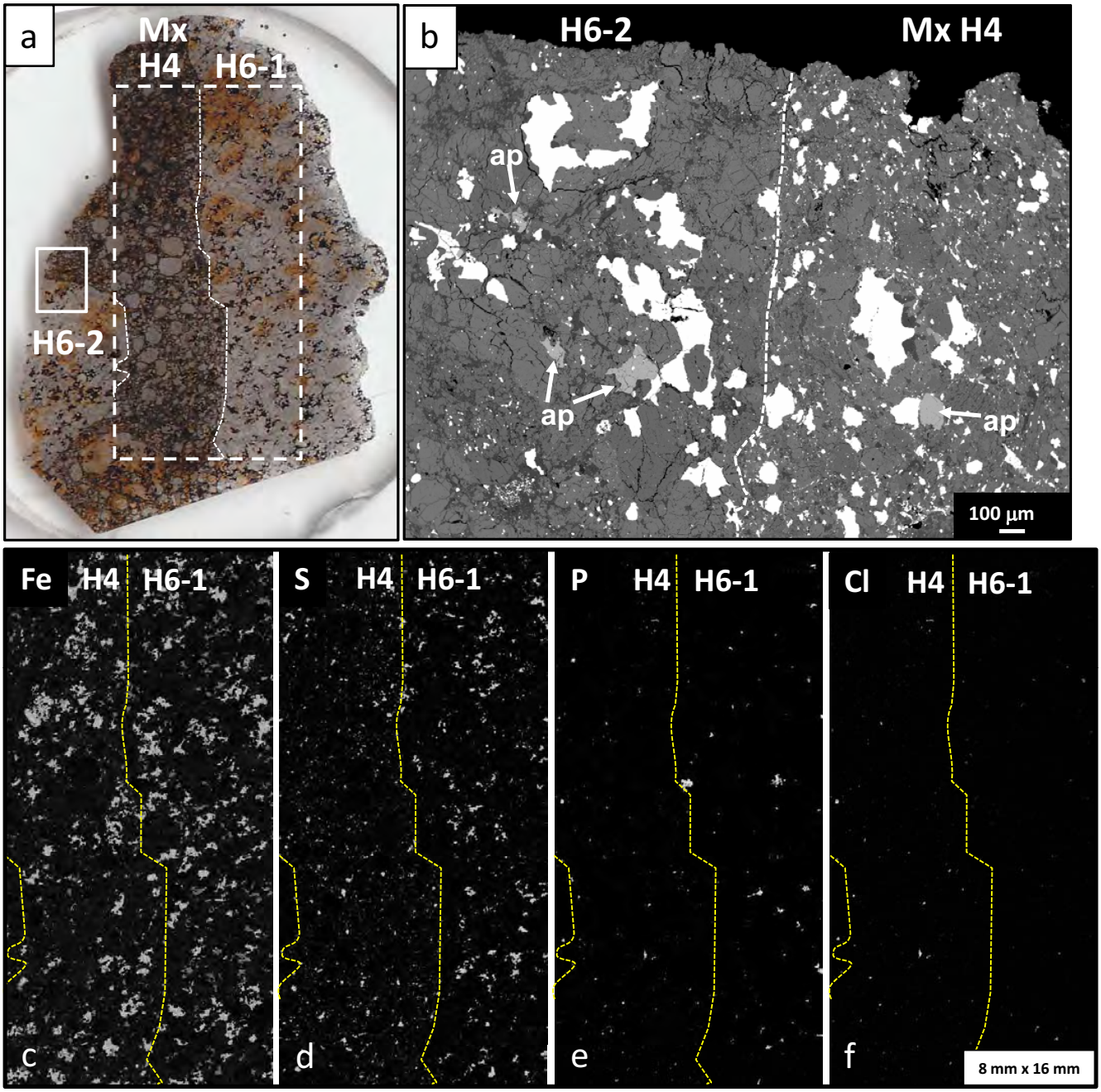

Fig. 7

Zag

This is a preprint, the final version is subject to change, of the American Mineralogist (MSA)
Cite as Authors (Year) Title. American Mineralogist, in press.
(DOI will not work until issue is live.) DOI: http://dx.doi.org/10.2138/am-2016-5728

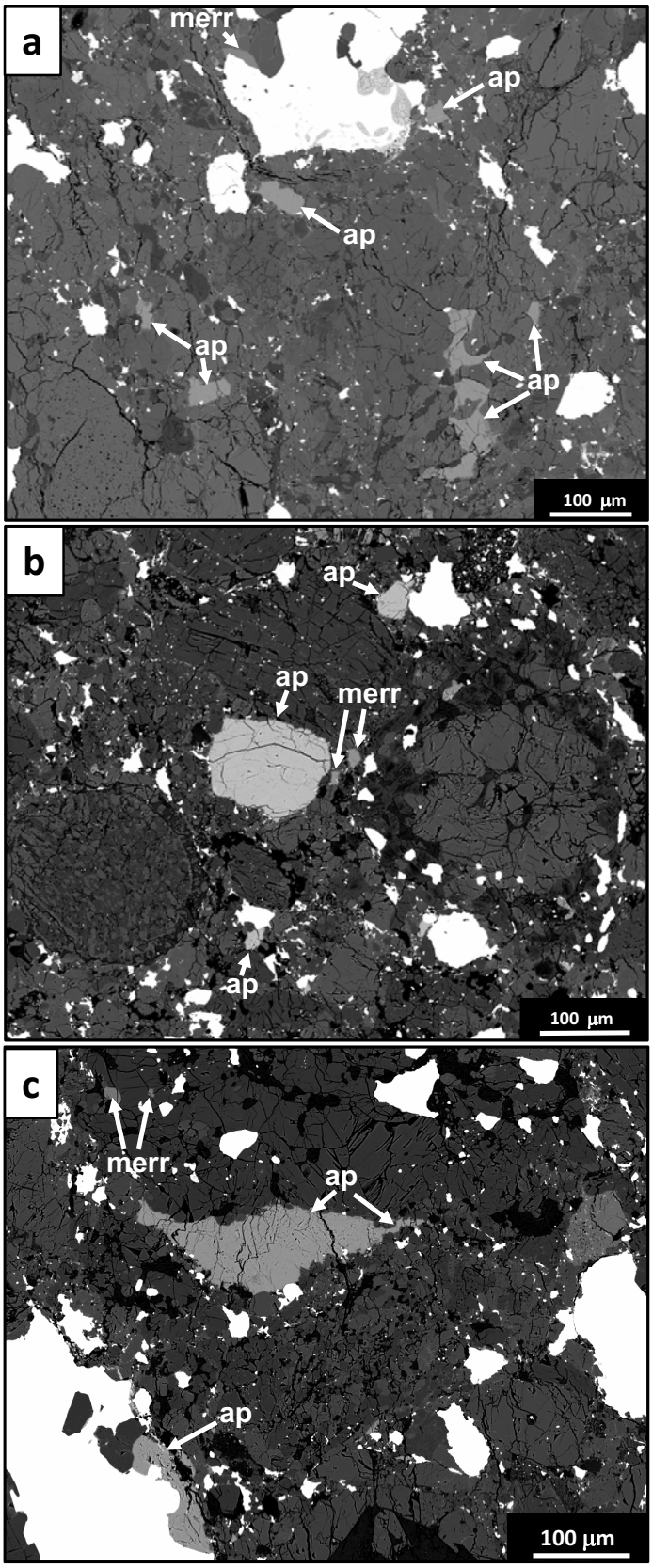

Fig. 8

Zag: H4 matrix

This is a preprint, the final version is subject to change, of the American Mineralogist (MSA)
Cite as Authors (Year) Title. American Mineralogist, in press.
(DOI will not work until issue is live.) DOI: http://dx.doi.org/10.2138/am-2016-5728

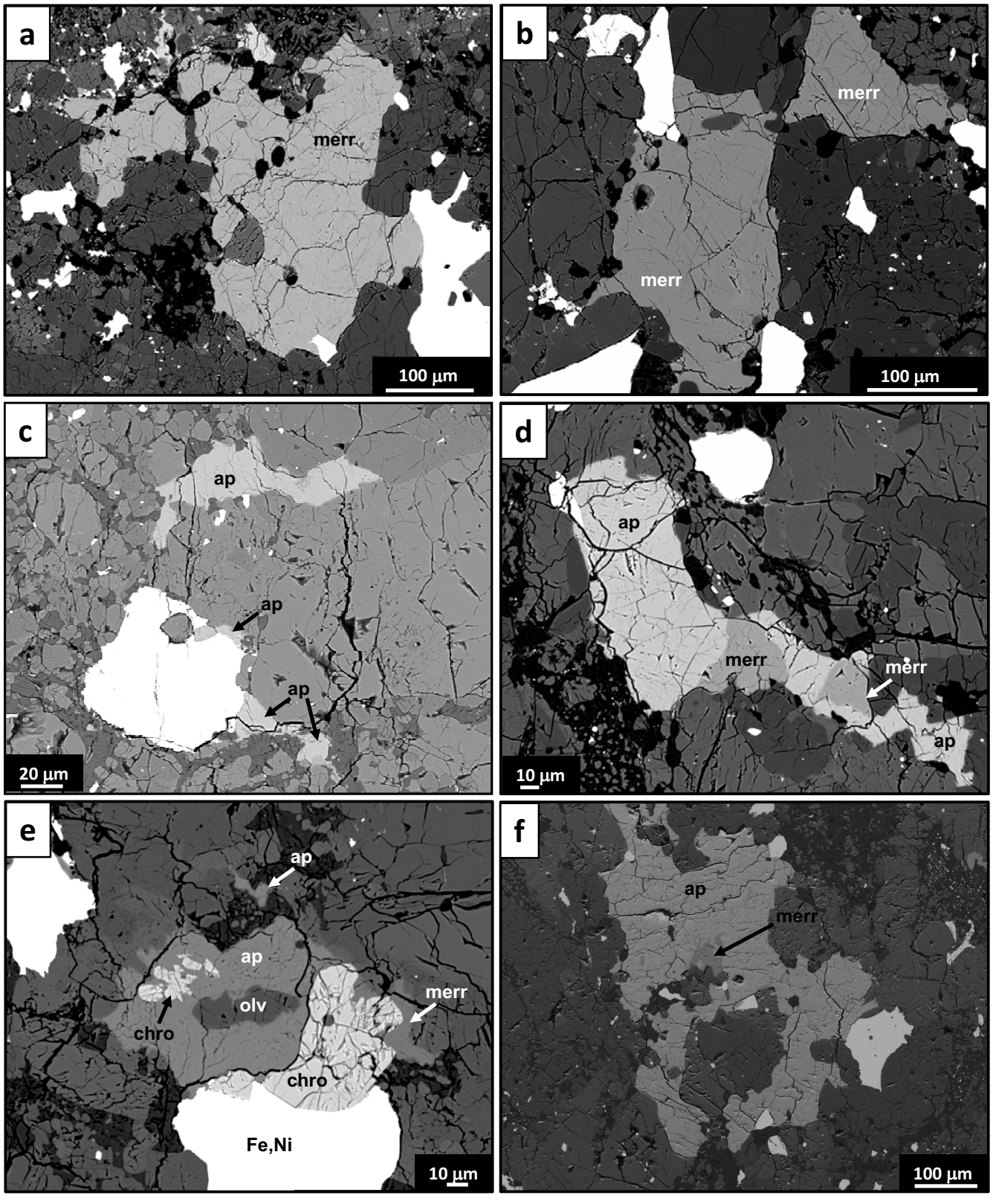

Fig. 9

Zag: a-e) H6-1; f) H6-2

This is a preprint, the final version is subject to change, of the American Mineralogist (MSA)
Cite as Authors (Year) Title. American Mineralogist, in press.
(DOI will not work until issue is live.) DOI: http://dx.doi.org/10.2138/am-2016-5728

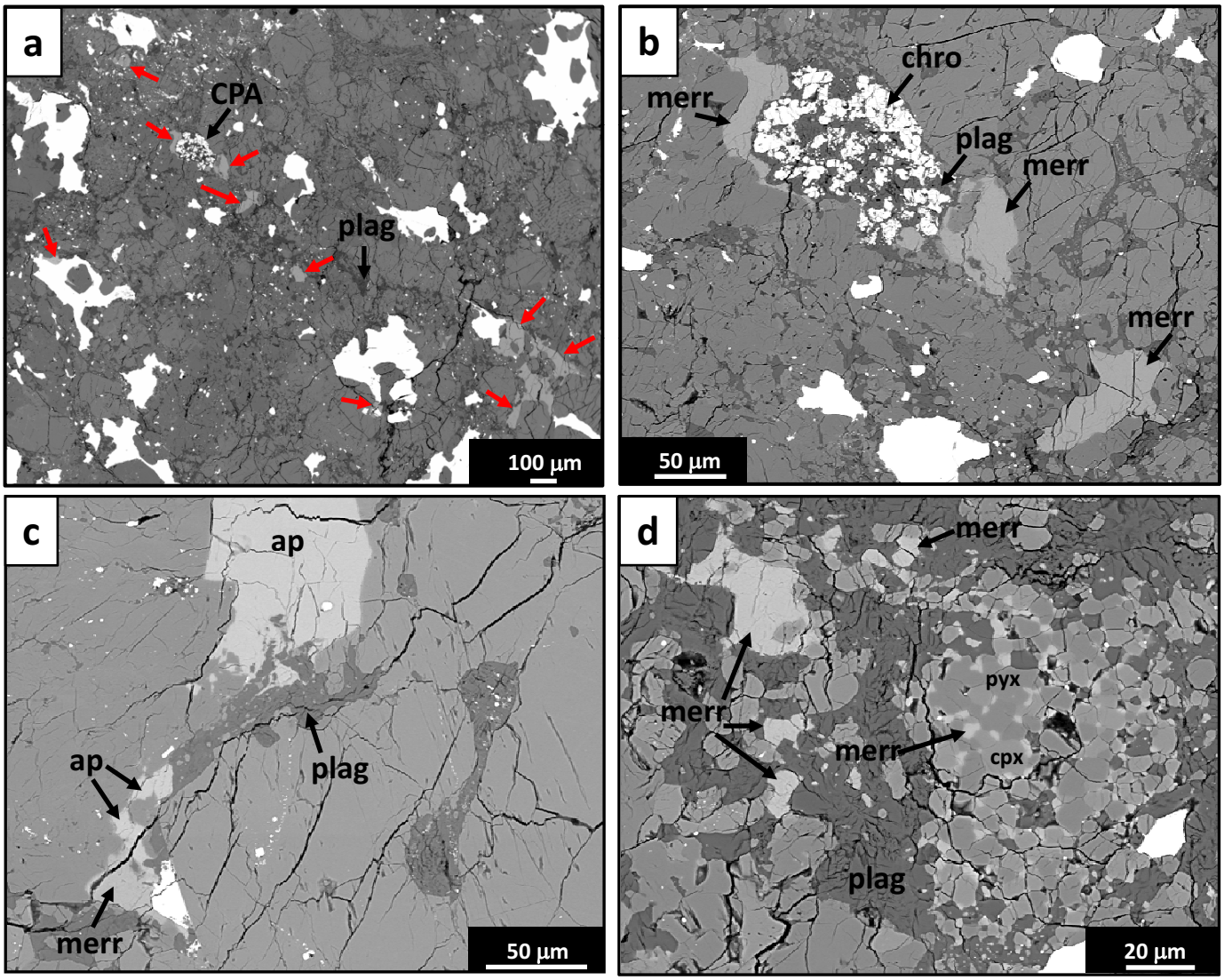

Fig. 10

Zag: H6-1